Noname manuscript No.
(will be inserted by the editor)

IMPLICATIONS OF X-RAY OBSERVATIONS FOR ELECTRON ACCELERATION AND PROPAGATION IN SOLAR FLARES

G.D. HOLMAN[1], M.J. ASCHWANDEN[2], H. AURASS[3], M. BATTAGLIA[4], P.C. GRIGIS[5], E.P. KONTAR[6], W. LIU[7], P. SAINT-HILAIRE[8], V.V. ZHARKOVA[9]

March 10, 2008

Abstract High-energy X-rays and γ-rays from solar flares were discovered fifty years ago. Since that time, the standard for the interpretation of spatially integrated flare X-ray spectra at energies above several tens of keV has been the collisional thick-target model. After the launch of the Ramaty High Energy Solar Spectroscopic Imager (RHESSI) in early 2002, X-ray spectra and images have been of sufficient quality to allow a greater focus on the energetic electrons responsible for the X-ray emission, including their origin and their interactions with the flare plasma and magnetic field. The result has been new insights into the flaring process, as well as more quantitative models for both electron acceleration and propagation, and for the flare environment with which the electrons interact. In this article we review our current understanding of electron acceleration, energy loss, and propagation in flares. Implications of these new results for the collisional thick-target model, for general flare models, and for future flare studies are discussed.

Keywords Sun: flares, Sun: X-rays, gamma rays, Sun: radio radiation

Contents

[1] NASA Goddard Space Flight Center, Code 671, Greenbelt, MD 20771, U.S.A. E-mail: Gordon.D.Holman@nasa.gov
[2] Lockheed Martin Advanced Technology Center, Solar and Astrophysics Laboratory, Organization ADBS, Building 252, 3251 Hanover Street, Palo Alto, CA 94304, U.S.A.
[3] Astrophysikalisches Institut Potsdam
[4] Institute of Astronomy, ETH, Zurich
[5] Harvard-Smithsonian Center for Astrophysics P-148, 60 Garden St., Cambridge, MA 02138, U.S.A.
[6] Department of Physics and Astronomy, University of Glasgow, Kelvin Building, Glasgow, G12 8QQ, U.K.
[7] NASA Goddard Space Flight Center, Code 671, Greenbelt, MD 20771, U.S.A.
[8] Space Sciences Lab, UC Berkeley, CA, U.S.A.
[9] Department of Computing and Mathematics, University of Bradford, Bradford, BD7 1DP, UK

1 Introduction

A primary characteristic of solar flares is the acceleration of electrons to high, suprathermal energies. These electrons are observed directly in interplanetary space, and indirectly at the Sun through the X-ray, γ-ray, and radio emissions they emit. Understanding how these electrons are produced and how they evolve is fundamental to obtaining an understanding of energy release in flares. Therefore, one of the principal goals of solar flare research is to determine when, where, and how these electrons are accelerated to suprathermal energies, and what happens to them after they are accelerated to these high energies.

A major challenge to obtaining an understanding of electron acceleration in flares is that the location where they are accelerated is not necessarily where they are most easily observed. The flare-accelerated electrons that escape the Sun are not observed until they reach the satellite-borne instruments capable of detecting them, usually located at the distance of the Earth from the Sun. The properties of these electrons are easily modified during their long journey from the flaring region to the detecting instruments. The electrons that are observed at the Sun through their X-ray or γ-ray emissions radiate most intensely where the density of the ambient plasma is highest. Therefore, the radiation from electrons in and near the acceleration region may not be intense enough to be observable. Although these radiating electrons are much closer to the acceleration region than those detected in interplanetary space, their properties can still be significantly modified as they propagate to the denser regions where they are observed. The radio emission from the accelerated electrons also depends on the plasma environment, especially the magnetic field strength for the gyrosynchrotron radiation observed from flares. Therefore, determining when, where, and how the electrons were accelerated requires a substantial amount of deductive reasoning.

Here we focus primarily on the X-ray emission from the accelerated electrons. Interplanetary electrons are addressed in Fletcher et al (2008), while the γ-ray emission is addressed in Vilmer et al (2008) and the radio in White et al (2008). The X-rays are primarily electron-ion bremsstrahlung (free-free radiation), emitted when the accelerated electrons scatter off ions in the ambient thermal plasma. Issues related to the emission mechanism and deducing the properties of the emitting electrons from the X-ray observations are addressed in Kontar et al (2008). Here we address the interpretation of the X-ray observations in terms of flare models and consider the implications of the observations for the acceleration process, energy release in flares, and electron propagation. Specific models for particle acceleration and energy release in flares are addressed in Vlahos et al (2008).

The X-ray emission is greatest when the collisions with ambient ions are so frequent that energy losses resulting from collisions with ambient electrons are also significant. These losses in turn change the energy distribution of the radiating electrons. When the accelerated electrons lose all their suprathermal energy to the ambient plasma while radiating, the source region is called a “thick target.” Electrons streaming downward into the higher densities in lower regions of the solar atmosphere, or trapped long enough in lower density regions, will emit thick-target X-rays. Hence, thick-target models are important to understanding

the origin and evolution of accelerated electrons in flares. Thick-target X-ray emission is addressed in Section 2.

The total energy carried by accelerated electrons is important to assessing acceleration models. Also, the energy carried by electrons that escape the acceleration region is deposited elsewhere, primarily to heating the plasma in the thick-target source regions. The energy carried by the accelerated electrons is sensitive to the value of the low-energy cutoff to the electron distribution. The determination of this low-energy cutoff and the energy in the accelerated electrons is addressed in Section 3.

In the standard thick-target model, the target plasma is assumed to be fully ionized. If the target ionization is not uniform, so that the accelerated electrons stream down to cooler plasma that is partially ionized or un-ionized, the X-ray spectrum is modified. This is addressed in Section 4.

Observations of the radiation from hot flare plasma have shown this plasma to primarily be confined to magnetic loops or arcades of magnetic loops. The observations also indicate that the heating of this plasma and particle acceleration initially occur in the corona above these hot loops (see Fletcher et al 2008). When the density structure in these loops is typical of active region loops, or at least not highly enhanced above those densities, the highest intensity, thick-target X-ray emission will be from the footpoints of the loops, as is most often observed to be the case. If accelerated electrons alone, unaccompanied by neutralizing ions, stream down the legs of the loop from the acceleration region to the footpoints, they will drive a co-spatial return current in the ambient plasma to neutralize the high current associated with the electron beam. The electric field associated with this return current will decelerate electrons in the beam, which can in turn modify the X-ray spectrum from the accelerated electrons. This is addressed in Section 5.

Collisional energy losses become apparent first for lower energy electrons. Therefore, for suprathermal electrons streaming downward to the footpoints of a loop, the footpoint X-ray sources observed at lower energies should be higher than footpoint sources observed at higher X-ray energies. The height dispersion of these sources provides information about the height distribution of the plasma density in the footpoints. The spatial resolution of the Ramaty High Energy Solar Spectroscopic Imager (RHESSI) has made such a study possible. This is described in Section 6. RHESSI has observed X-ray sources move downward from the loop top and upward from the footpoints during some flares. This source evolution is also discussed here.

Since higher energy electrons have higher velocities than lower energy electrons, the footpoint X-ray emission from the higher energy electrons should arrive earlier than that from lower energy electrons. The length of this time delay provides an important test for the height of the acceleration region. Longer time delays can result from magnetic trapping of the electrons. The evolution of the thermal plasma in flares can also exhibit time delays associated with the balance between heating and cooling processes. These various time delays and the information they provide are addressed in Section 7.

An important diagnostic of electron acceleration and propagation in flares is the time evolution of the X-ray spectrum during flares. In most flares, for example, the X-ray spectrum becomes harder (flatter, smaller spectral index) and then softer (steeper, larger spectral index) as the X-ray flux evolves from low to high and then back to low. Spectral evolution is addressed in Section 8.

One of the most important results from the *Yohkoh* mission was the discovery of a hard (high energy) X-ray source above the top of of the thermal (low energy) X-ray loops. This, together with the *Yohkoh* observations of cusps at the top of flare X-ray loops, provided strong evidence that energy release occurs in the corona above the hot X-ray loops (for some

flares, at least). Although several models have been proposed, the origin of these "above-the-loop-top sources" is not well understood. To better understand these sources, we need to understand how their properties and evolution compare to the more common footpoint hard X-ray sources. These issues are addressed in Section 9.

As mentioned at the top of this section, radio observation provide another view of accelerated electrons and related flare phenomena. Although radio observations and their relationship to flare X-ray emission are primarily addressed in White et al (2008), some intriguing radio observations that bear upon electron acceleration in flares are presented in Section 10.

As is typical for a successful mission, RHESSI observations of flare X-ray emission have led to both substantial progress and many unanswered questions. Part of the progress is that many of the questions are different from those that were asked less than a decade ago. The primary context for interpreting the X-ray emission from suprathermal electrons is the thick-target model, while the ultimate goal is to understand how the electrons are accelerated. In Section 11 we summarize and discuss the implications of the X-ray observations for the thick-target model and electron acceleration mechanisms, and highlight some of the questions that remain to be answered.

2 Thick-target X-ray emission

As was summarized in Section 1, the electron-ion bremsstrahlung X-rays from a beam of accelerated electrons will be most intense where the density of target ions is highest, as well as where the flux of accelerated electrons is high. The local emission (emissivity) of photons of energy ε by electrons of energy E is given by the product of the plasma ion density, $n(\mathbf{r})$, times the electron beam flux density distribution, $F(\mathbf{r},E)$ (electrons cm $^{-2}$ s^{-1} keV^{-1}), times the electron-ion bremsstrahlung cross section, $Q(\varepsilon,E)$. For simplicity, we do not consider here the angular distribution of the beam electrons or the emitted photons, topics addressed in Kontar et al. (Chapter 7).

The emissivity of the radiation at energy ε from all the electrons in the beam is obtained by integrating over all contributing electron energies, which is all electron energies above the photon energy. The photon flux emitted per unit energy is obtained by integrating over the emitting source volume (V) or, for an imaged source, along the line of sight through the source region. Finally, assuming isotropic emission, the observed spatially integrated flux density of photons of energy ε at the X-ray detector, $I(\varepsilon)$ photons cm $^{-2}$ s^{-1} keV^{-1}, is simply the flux divided by the geometrical dilution factor $4\pi R^2$, where R is the distance to the X-ray detector:

$$I(\varepsilon) = \frac{1}{4\pi R^2} \int_V \int_\varepsilon^\infty n(\mathbf{r}) F(E,\mathbf{r}) Q(\varepsilon,E)\, dE\, dV. \tag{2.1}$$

We refer to $I(\varepsilon)$ as the X-ray flux spectrum, or simply the X-ray spectrum. The spectrum obtained directly from an X-ray detector is generally a count spectrum, which must be converted to an X-ray flux spectrum by correcting for the detector response (see, for example, Smith et al. 2002).

Besides increasing the X-ray emission, a high plasma density also means increased energy losses for the beam electrons. In a dense plasma the bremsstrahlung losses are dominated by collisional losses to the plasma electrons. For a fully ionized plasma, the (nonrelativistic) loss rate is

$$dE/dt = -(K/E)\, n(\mathbf{r})\, v(E), \tag{2.2}$$

where $K = 2\pi e^4 \Lambda_{ee} \approx 2.6 \times 10^{-18}$ cm^2 keV^2, Λ_{ee} is the Coulomb logarithm, and $v(E)$ is the speed of the electron (Brown 1971, Kontar et al. – Chapter 7). Noting that $vdt = dz$, equation 2.2 can be simplified to $dE/dN = -K/E$, where N(z) (cm $^{-2}$) is the column density. Hence, the evolution of an electron's energy with column density is simply

$$E^2 = E_0^2 - 2KN, \tag{2.3}$$

where E_0 is the initial (injected) energy of the electron.

If energy losses are not significant within an X-ray source, the emission is called "thin-target." If, on the other hand, the nonthermal electrons lose all their suprathermal energy within a spatially unresolved source region, the emission is called "thick-target." The maximum information that can be obtained about the accelerated electrons from an X-ray spectrum alone is contained in the "mean electron flux" distribution (see Kontar et al., Chapter 7). Additional information is required to determine if the X-ray emission is thin-target, thick-target, or something in between. The flux distribution of the emitting electrons and the mean electron flux distribution are equivalent for a homogeneous, thin-target source region.

Equation 2.1 gives the observed X-ray flux in terms of the accelerated electron flux density distribution throughout the source. However, we are interested in the electron distribution injected into the source, $F_0(\mathbf{r_0}, E_0)$. To obtain this, we need to know how to relate $F(\mathbf{r}, E)$ at all locations within the source region to $F_0(\mathbf{r_0}, E_0)$. Since we are interested in the X-rays from a spatially integrated, thick-target source region, the most direct approach is to first compute the bremsstrahlung photon yield from a single electron of energy E_0, $v(\varepsilon, E_0)$ (Brown 1971). As long as the observational integration time is longer than the time required for the electrons to radiate all photons of energy ε, the thick-target X-ray spectrum is then given by

$$I_{thick}(\varepsilon) = \frac{1}{4\pi R^2} \int_{\varepsilon}^{\infty} \mathscr{F}_0(E_0)\, v(\varepsilon, E_0)\, dE_0, \tag{2.4}$$

where $\mathscr{F}_0(E_0)$ is the electron beam flux distribution (electrons s $^{-1}$ keV^{-1}).

The rate at which an electron of energy E radiates bremsstrahlung photons of energy ε is $n(\mathbf{r})v(E)Q(\varepsilon, E)$. The photon yield is obtained by integrating this over time. Since the electrons are losing energy at the rate dE/dt, the time integration can be replaced by an integration over energy from the initial electron energy E_0 to the lowest energy capable of radiating a photon of energy ε:

$$v(\varepsilon, E_0) = \int_{E_0}^{\varepsilon} \frac{n(\mathbf{r})\, v(E)\, Q(\varepsilon, E)\, dE}{dE/dt}. \tag{2.5}$$

Using equation 2.2 for dE/dt, equation 2.4 becomes

$$I_{thick}(\varepsilon) = \frac{1}{4\pi R^2} \frac{1}{K} \int_{E_0=\varepsilon}^{\infty} \mathscr{F}_0(E_0) \int_{E=\varepsilon}^{E_0} E\, Q(\varepsilon, E)\, dE\, dE_0. \tag{2.6}$$

Note that the thick-target X-ray flux spectrum does not depend on the plasma density. However, the plasma must be dense enough for the emission to be thick-target. Integration of equation 2.2 shows that this typically implies a plasma density $\sim 10^{11} - 10^{12}$ cm^{-3} for an observational integration time of 1 s (see Sections 9.4 and 11.1 for more about this).

Observed X-ray spectra from solar flares can usually be well fitted with a model photon spectrum that is either a single or a double power-law. For a single power-law electron flux distribution of the form $\mathscr{F}(E) \propto E^{-\delta}$, the photon spectrum also has the power-law form $I(\varepsilon) \propto \varepsilon^{-\gamma}$. The relationship between the electron and photon spectral indices δ and γ can

most easily be obtained from equations 2.1 and 2.6 using the Kramers approximation to the bremsstrahlung cross section: $Q(\varepsilon,E) \propto 1/\varepsilon E$. For a simple thin-target source,

$$I_{thin}(\varepsilon) \propto \varepsilon^{-(\delta+1)}, \tag{2.7}$$

giving $\gamma_{thin} = \delta + 1$. For a thick-target source region,

$$I_{thick}(\varepsilon) \propto \varepsilon^{-(\delta-1)}, \tag{2.8}$$

giving $\gamma_{thick} = \delta - 1$. Analytic expressions relating the normalization coefficients can also be obtained when the non-relativistic Bethe-Heitler bremsstrahlung cross section is valid (Brown 1971; Tandberg-Hanssen and Emslie 1988). These simple power-law relationships are *not valid* if there is a break or a cutoff in the electron distribution above the energies of interest. For example, these relationships are not correct for the lower power-law index of a double power-law fit to a photon spectrum. Equation 2.1 or 2.6 can be used to numerically compute the X-ray spectrum from an arbitrary flux distribution in electron energy.

It is important to recognize that the above power-law relationships are only valid if the electron flux density or electron flux distribution is assumed to have a power-law energy dependence. It is sometimes convenient to work with the electron *density distribution*, $f(\mathbf{r},E)$ (electrons cm^{-3} keV^{-1}), rather than the *flux density distribution*, especially when considering thin-target emission alone or comparing X-ray spectra with radio spectra. The flux density and density distributions are related through $F(\mathbf{r},E) = f(\mathbf{r},E)v(E)$. If the electron density distribution rather than the flux distribution is assumed to have a power-law index δ' ($f(E) \propto E^{-\delta'}$), the relationships between this power-law index and the photon spectral index become $\gamma_{thin} = \delta' + 0.5$ and $\gamma_{thick} = \delta' - 1.5$.

3 Low-energy cutoffs and the energy in nonthermal electrons

3.1 Why do we need to determine the low-energy cutoff of nonthermal electron distributions?

An important feature of the thick-target model is that the photon spectrum $I(\varepsilon)$ is directly determined by the injected electron flux distribution $\mathscr{F}_0(E_0)$. As can be seen from equation 2.6, no additional parameters such as source density or volume need to be determined. Consequently, by integrating over all electron energies, we can also determine the total flux of nonthermal electrons, N_{nth} electrons s^{-1}, the power in nonthermal electrons, P_{nth} erg s^{-1}, and, integrating over time, the total number of and energy in nonthermal electrons.

The total nonthermal electron number flux and power are computed as follow:

$$N_{nth} = \int_{E_c}^{+\infty} \mathscr{F}_0(E_0)\,dE_0 = \frac{A}{\delta-1} {E_c}^{-\delta+1} \tag{3.1}$$

$$P_{nth} = \kappa_E \int_{E_c}^{+\infty} E_0 \cdot \mathscr{F}_0(E_0)\,dE_0 = \frac{\kappa_E A}{\delta-2} {E_c}^{-\delta+2} \tag{3.2}$$

The last expression in each equation is the result for a power-law electron flux distribution of the form $\mathscr{F}_0(E_0) = A \cdot E_0^{-\delta}$. The constant $\kappa_E = 1.6 \times 10^{-9}$ is the conversion from keV to erg. E_c is a low-energy cutoff to the electron flux distribution.

The non-thermal *power* (and of course ultimately, the non-thermal *energy*) from the power-law electron flux distribution depends on three parameters: δ, A, and E_c. Observations indicate that δ is almost always greater than 2 (Dennis 1985; Lin and Schwartz 1987;

Winglee et al. 1991; Holman et al. 2003). Hence, were E_c=0, the integral would yield an infinite value, a decidedly unphysical result! Therefore, the power-law electron distribution cannot extend all the way to zero energy, and some form of a *low-energy cutoff* in the accelerated electron spectrum must be determined. As we will see, this is not a straightforward process, but is the single most important parameter to determine (as the other two are generally more straightforward to determine — see Section 2 and Kontar et al., Chapter 7). For example with δ=4 (typical during the peak time of strong flares), a factor of 2 error in E_c yields a factor of 4 error in P_{nth}. For larger δ (as found in small flares, or rise/decay phases of large flares), such an error quickly leads to an order of magnitude (or even greater) difference in the injected power P_{nth}!

3.2 Why is the low-energy cutoff difficult to determine?

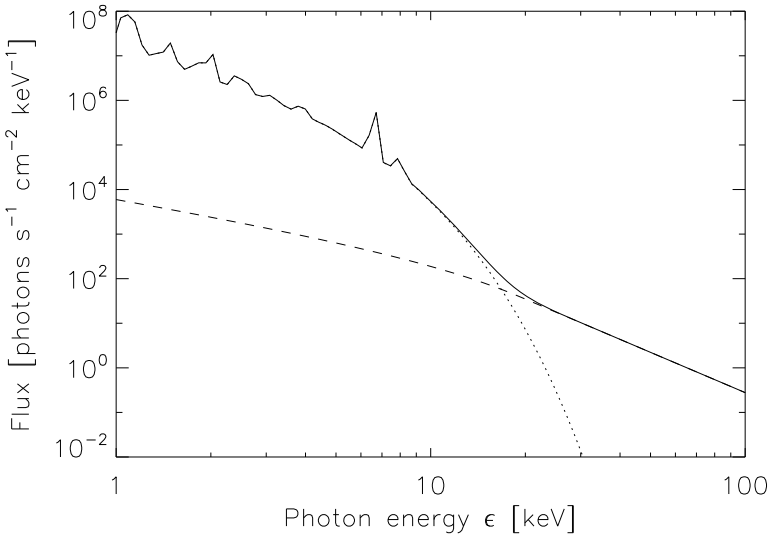

Fig. 3.1 Typical full-sun flare spectrum. *Dashed:* Non-thermal spectrum from an accelerated electron distribution with δ=4, and a low-energy cutoff of 20 keV. *Dotted:* Thermal spectrum, from a plasma with temperature $T = 20$ MK and emission measure $EM = 10^{49}$ cm^{-3}. *Solid:* Total radiated spectrum.

The essence of the problem in many flare spectra is summarized in Fig. (3.1): the non-thermal power-law is well-observed above $\sim$20 keV, but any revealing features that it might possess at low energies, such as a low-energy cutoff, are washed out by the presence of the thermal emission.

Even if a spectrum does show a flattening at low energies that could be the result of a low-energy cutoff, other mechanisms that could produce the flattening must be ruled out (see Section 3.4). The low-energy cutoff has the unique feature that the X-ray spectrum eventually approaches a spectral index of 1 at low energies (cf., Holman 2003). It is difficult, however, to observe a spectrum to low enough photon energies to see that the spectrum does

indeed become this flat. Generally we can only hope to rule out the other mechanisms based on additional data and detailed spectral fits.

3.3 What is the shape of the low-energy cutoff, and how does it impact the photon spectrum and P_{nth}?

Bremsstrahlung photon spectra are obtained from convolution integrals over the electron flux distribution (equations 2.1 and 2.6). Hence, features in an electron distribution tend to be smoothed out in the resulting photon spectrum (see e.g., Brown et al. 2006).

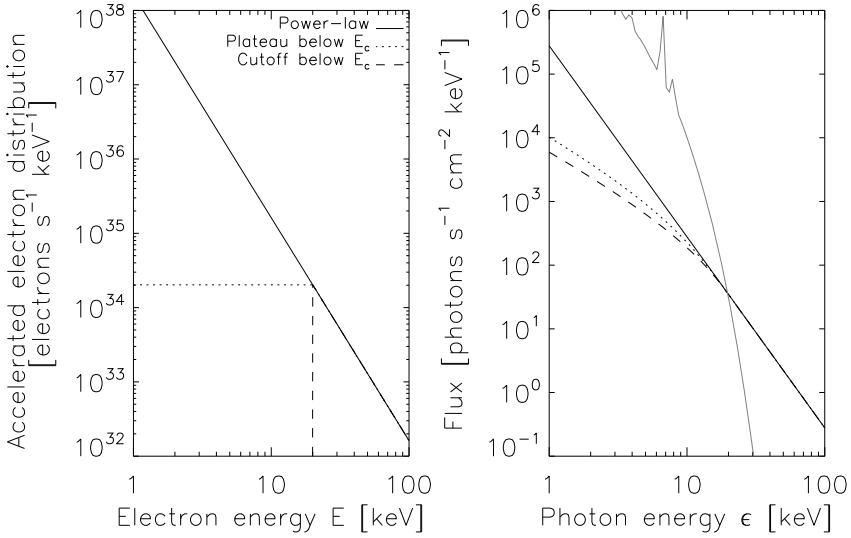

Fig. 3.2 Different shapes of low-energy cutoff in the injected electron distribution *(left)* lead to slightly different photon spectra *(right)*. The cutoff/turnover electron energy is E_c=20 keV. The thin curve in the right panel demonstrates how the cutoff can be masked by emission from thermal plasma. See also Holman (2003) for a thorough discussion of bremsstrahlung spectra generated from electron power-laws with cutoff.

As can be seen in Fig. (3.2), both a sharp cutoff and a "turnover" (defined here to be a constant $F_0(E)$ below E_c) feature for the injected electron distribution lead to somewhat similar thick-target photon spectra. This subtle difference is difficult to discriminate, and the problem is compounded by masking by a strong thermal component.

A sharp cutoff would lead to plasma instabilities that should theoretically destroy the distribution within a few nanoseconds ("bump-on-tail" instability). On the other hand, the spectrum below the cutoff must be flatter than E^{-1}, as demonstrated by equation 3.1, or the total electron flux would be infinite. Having a constant value for the distribution below E_c (turnover case) seems like a reasonable middle ground and approximates a quasilinearly relaxed electron distribution (e.g., Krall and Trivelpiece 1973, Chapter 10). Coulomb collisional losses, on the other hand, yield an electron distribution that increases linearly at low energies (see Fig. 3.3), leading to a photon spectrum between the sharp cutoff case and the turnover case.

Notice that the photon spectra actually flatten gradually to the spectral index of 1 at low energies from the spectral index of $\gamma = \delta + 1$ at E_c and higher energies. Below E_c, it is *not* a power-law. Fitting a double power-law model photon spectrum, and using the break (i.e., kink) energy as the low-energy cutoff typically leads to a large error in E_c (e.g., Gan et al. 2001; Saint-Hilaire and Benz 2005), and hence to an even larger error in P_{nth}.

In terms of the energetics, Saint-Hilaire and Benz (2005) have shown that the choice of an exact shape for the low-energy cutoff as a model is not dramatically important. For a fixed cutoff energy, from equation 3.2 it can be shown that the ratio of the power in the turnover model to the power in the sharp cutoff model without the flat component below the cutoff energy is $\delta/2$. In obtaining spectral fits, however, the turnover model gives higher cutoff energies than the sharp cutoff model. Using simulations, Saint-Hilaire and Benz (2005) found that assuming either a sharp cutoff model or a turnover model led to differences in P_{nth} typically less than $\sim$20%. Hence, the sharp cutoff, being the simplest, is the model of choice for computing flare energetics. Nevertheless, knowing the exact shape of the low-energy cutoff not only yields more accurate non-thermal energy estimates, but can be a source of information on the acceleration mechanism and/or propagation effects.

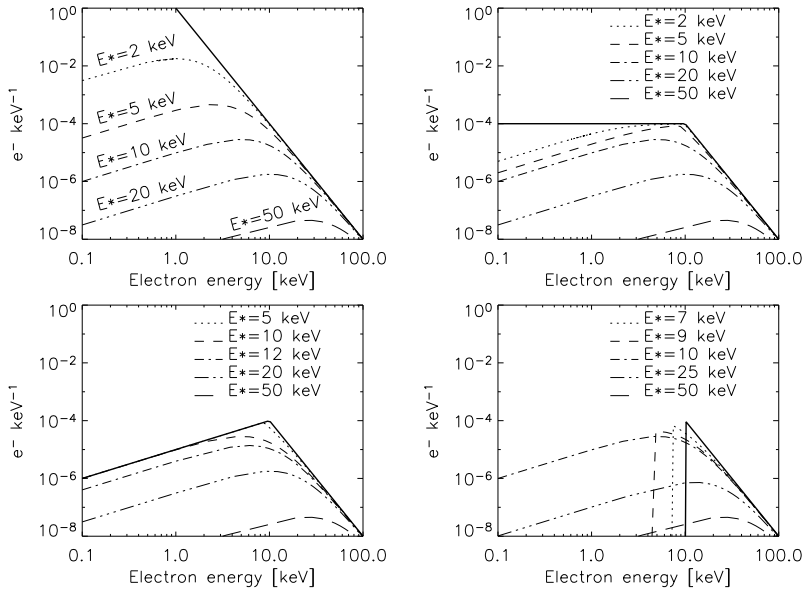

Fig. 3.3 The four plots show the Coulomb-collisional evolution with column density of an injected electron distribution (*thick, solid line*). For the simple power-law case (*upper left*), the low-energy end of the distribution becomes linear, and the peak of the distribution is found at $E_{peak} = E_*/\sqrt{\delta}$, where δ is the injected distribution power-law spectral index (δ=4 in the plots), and $E_* = \sqrt{2K \cdot N_*}$ is the initial energy that electrons must possess in order not to be fully stopped by a column density N_* (Eq. 2.3). When a low-energy cutoff is present, the peak of the distribution is seen to first decreases in energy until E_* exceeds the cutoff energy.

Spectral inversion methods have recently been developed (cf. Brown et al. 2006) for deducing the *plasma density weighted, target-averaged electron flux density distribution* (Johns & Lin, 1992), also known as the *mean electron flux distribution* (Brown et al. 2003), from X-ray spectra. A spectral "dip" has been found just above the presumed thermal com-

ponent in some deduced mean electron flux distributions that may be associated with a low-energy cutoff (e.g., Piana et al. 2003). In the collisional thick-target model, the slope of the high-energy "wall" of this dip should be linear of flatter, with a linear slope indicating the absence of emitting electrons in the injected electron distribution at the energies displaying this slope. Kontar and Brown (2006) have found evidence for slopes that are steeper than linear. Finding and understanding these dips is a crucial element for gaining an understanding of the low-energy properties of flare electron distributions (see Chapter 7).

Emslie (2003) has pointed out that nonthermal electron distribution could seamlessly merge into the thermal distribution, removing the need for a low-energy cutoff. As was shown by Holman et al. (2003) for the 2002 July 23 flare, however, merger of the electron distribution into the typically derived $\sim$10–30 MK thermal flare plasma generally implies an exceptionally high energy in nonthermal electrons. Thus, for a more likely energy content, a hotter plasma would need to be present in the target region. Any emission from this "hot core", because of its much lower emission measure, is likely to be masked by the usual $\sim$10–30 MK thermal emission. This merger of the nonthermal electron distribution into the thermal tail in the target region does not remove the need for a low-energy cutoff in the electrons that escape the acceleration region, unless these electrons are accompanied by hot, thermal plasma electrons.

This section has dealt with the shape of the low-energy cutoff. It had assumed that the photon spectra are not altered by other mechanisms, and that the bremsstrahlung emission was isotropic. The next section lists the important caveats to these assumptions, and their possible influence in the determination of low-energy cutoffs.

3.4 Important caveats

As previously discussed, apparently minor features in the bremsstrahlung photon spectrum can have substantial implications for the mean electron flux and, consequently, the injected electron distribution. This means that unknown or poorly-understood processes that alter the injected electron distribution (propagation effects, for example) or the photon spectrum (including instrumental effects) can lead to significant errors in the determination of the low-energy cutoff. Known processes that affect the determination of the low-energy cutoff are enumerated below.

1. Detector pulse pile-up effects (Smith et al. 2002), if not properly corrected for, can introduce a flattening of the spectrum toward lower energies that simulates the flattening resulting from a low-energy cutoff.
2. The contribution of Compton back-scattered photons (photospheric albedo) to an X-ray spectrum can simulate the spectral flattening produced by a low-energy cutoff. Kašparová et al. (2005) have shown that the dip in a spectrum from a flare on 2002 August 20 becomes statistically insignificant when the spectrum is corrected for photospheric albedo (also see Kontar et al 2008). Kašparová et al. (2007) show that spectra in the 15–20 keV energy band tend to be flatter near disk center when albedo from isotropically emitted photons is not taken into account, further demonstrating the importance of correcting for photospheric albedo.
3. The assumed differential cross-section and electron energy loss rate can influence the results (see Saint-Hilaire and Benz 2005, for a discussion). In some circumstances a contribution from recombination radiation may significantly change the results (see Kontar et al 2008).

4. Anisotropies in the electron beam directivity and the bremsstrahlung differential cross-section can significantly alter the spectrum (Massone et al. 2004).
5. Non-uniform target ionization (the fact that the chromosphere's ionization state varies with depth, see Section 4) can introduce a spectral break that may be confused with the break associated with a low-energy cutoff.
6. Energy losses associated with a return current produce a low-energy flattening of the X-ray spectrum (Section 5). This is a true low-energy "cut off" in the electron distribution, but occurs between the acceleration region and the emitting source region.

For all the above reasons, the exact shape and value of the low-energy cutoff in the injected electron spectrum is still not settled. The consensus in the solar physics community for now is to assume the simplest case, a sharp low-energy cutoff. Existing studies, presented in the next section, tend to support the adequacy of this assumption for current studies.

3.5 Determinations of E_c and electron energy content from flare data

Before RHESSI, instruments did not cover well (if at all) the $\sim$10–40 keV photon energies where the transition from thermal emission to nonthermal emission typically occurs. Researchers typically assumed an arbitrary low-energy cutoff at a value at or below the instrument's observing range (one would talk of the "injected power in electrons above E_c keV" instead of the total nonthermal power P_{nth}). An exception is Nitta et al. (1990). They argued that spectral flattening observed in two flares with the *Solar Maximum Mission* and *Hinotori* indicated a cutoff energy of $\gtrsim$50 keV. Also, Gan et al. (2001) interpreted spectral breaks in Compton GRO flare spectra as the low-energy cutoff in estimating flare energetics, resulting in rather small values for the nonthermal energy in the flares. The relatively low-resolution spectra from these instruments were not well constrained, however.

Benka and Holman (1994) applied a direct electric field electron acceleration model to the high-resolution balloon data of Lin et al. (1981) for the 1980 June 27 flare. They derived, along with other model-related parameters, the time evolution of of the critical energy above which runaway acceleration occurs – the model equivalent to the low-energy cutoff. Along with $\sim$25 microflares observed during the same balloon flight, this was the first and only high-resolution flare spectral data before the launch of RHESSI.

Thanks to RHESSI's high-spectral-resolution coverage of the 10–40 keV energy range and beyond, it is now possible in most cases to obtain a meaningful upper limit on E_c. Holman et al. (2003), Emslie et al. (2004), and Saint-Hilaire and Benz (2005), in determining the low-energy cutoff, obtained the "highest value for E_c that still fits the data": in many solar flare spectra, because of the dominance of radiation from thermal plasma at low energies, a range of values for E_c fit the data equally well, up to a certain critical energy, above which the χ^2 goodness-of-fit parameter becomes unacceptably large. The low-energy cutoff is taken to be equal to this critical value. This results in a lower limit for the non-thermal power and energy. The results obtained for the maximum value of E_c were typically in the 15–45 keV range, although late in the 2002 July 23 flare some values as high as $\sim$80 keV were obtained for E_c. The minimum nonthermal energies thus determined were comparable to or somewhat larger than the calculated thermal energies.

Sui et al. (2005a) complemented the spatially-integrated spectral data for the 2002 April 15 limb flare with imaging and lightcurve information, leading to one of the best determinations of the low-energy cutoff so far. Four spectra and spectral fits from this flare are shown in Fig. 3.4. The earliest spectrum, before the impulsive rise of the higher energy X-rays,

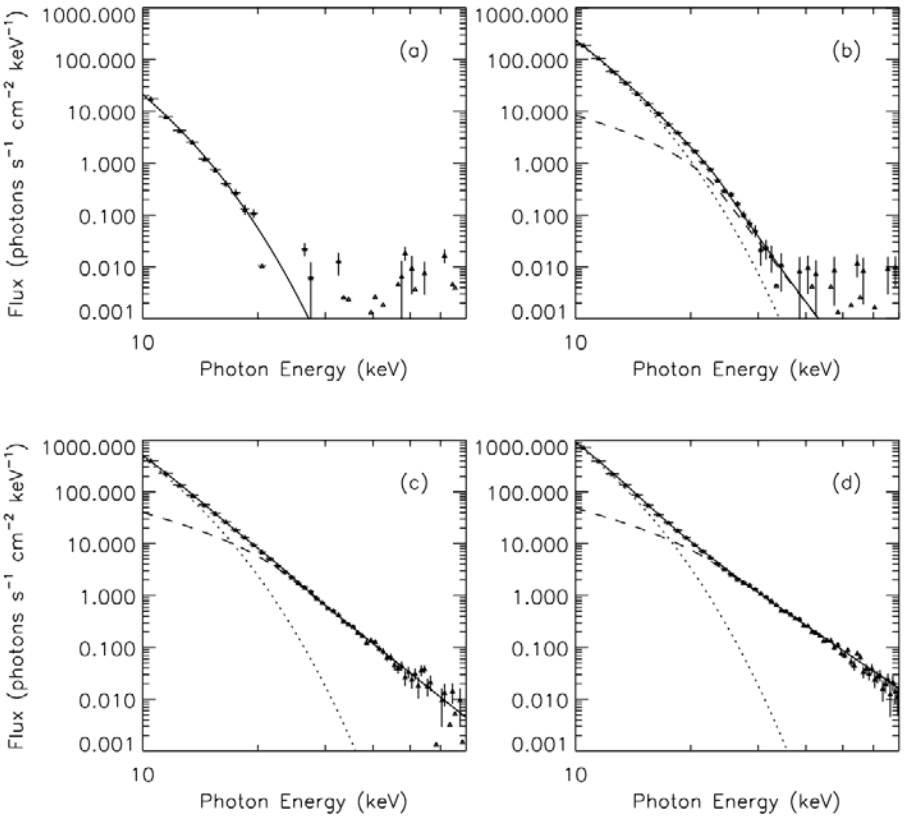

Fig. 3.4 RHESSI spatially integrated spectra in four time intervals during the 2002 April 15 flare. (a) Spectrum at 23:06:20–23:06:40 UT (early rise phase). (b) Spectrum at 23:09:00-23:09:20 UT (just before impulsive phase). (c) Spectrum at 23:10:00–23:10:20 UT (soon after the impulsive rise). (d) Spectrum at 23:11:00–23:11:20 UT (at the hard X-ray peak). The plus signs with error bars represent the spectral data. The lines represent model spectral fits: the dashed lines are nonthermal thick-target bremsstrahlung, the dotted lines are thermal bremsstrahlung, and the solid lines are the summation of the two (from Sui et al. 2005a).

was well fitted with an isothermal model. The last spectrum, from the time of the hard X-ray peak, clearly shows a thermal component below $\sim$20 keV. Of particular interest is the second spectrum, showing both thermal and nonthermal fit components. As a consequence of the flattening of the isothermal component at low energies, the low-energy cutoff to the nonthermal component cannot extend to arbitrarily low energies without exceeding the observed emission. This places a tight constraint on the value of the low-energy cutoff. The additional requirement that the time evolution of the derived temperature and emission measure of the thermal component be smooth and continuous throughout the flare constrains the value at other times. They found the best cutoff value to be $E_c = 24 \pm 2$ keV (roughly constant throughout the flare). The energy associated with these nonthermal electrons was found to be comparable to the peak energy in the X-ray-emitting thermal plasma, but an order of magnitude greater than the kinetic energy of the associated coronal mass ejection (Sui et al. 2005b).

Sui et al. (2007) did a search for low-energy cutoffs in the spectra of a sample of early impulsive flares observed by RHESSI in 2002. Early impulsive flares are flares in which

the >25 keV hard X-ray flux increase is delayed by less than 30 s after the flux increase at lower energies. The pre-impulsive-phase heating of plasma to X-ray-emitting temperatures is minimal in these flares. In the sample of 33 flares, 9 showed spectral flattening at low energies. After correcting for the albedo from isotropically emitted X-rays, the flattening in 3 of the 9 flares, all near Sun center, disappeared. The flattening that persisted in the remaining 6 flares was consistent with that produced by a low-energy cutoff. The authors found the evolution of the spectral break and the corresponding low-energy cutoff in these flares to be correlated with the hard X-ray flux. Further studies are needed to assess the significance of this correlation.

4 Nonuniform target ionization in the thick-target region

In the interpretation of hard X-ray (HXR) spectra in terms of the thick-target model, one effect which has been largely ignored until recently is that of varying ionization along the path of the thick target beam. As first discussed by Brown (1973), the decrease of ionization with depth in the solar atmosphere reduces long-range collisional energy losses. This enhances the HXR bremsstrahlung efficiency there, elevating the high energy end of the HXR spectrum by a factor of up to 2.8 above that for a fully ionized target. The net result is that a power-law electron spectrum of index δ produces a photon spectrum of index $\gamma = \delta - 1$ at low and high energies (see equation 2.8), but with $\gamma < \delta - 1$ in between. The upward knee, where the spectrum begins to flatten toward higher energies, occurs at fairly low energies, probably masked in data by the tail of the thermal component. The downward knee, where the spectrum steepens again to $\gamma = \delta - 1$, occurs in the few deka-keV range, depending on the column depth of the transition zone.

4.1 Electron energy losses and X-ray emission in a nonuniformly ionized plasma

The collisional energy-loss cross section $Q_c(E)$ is dependent on the ionization of the background medium. Flare-accelerated electron beams can propagate in the fully ionized corona as well as in the partially ionized transition region and chromosphere. Following Hayakawa and Kitao (1956) and Brown (1973), the cross-section $Q_c(E)$ can be written for a hydrogen plasma ionization fraction x

$$Q_c(E) = \frac{2\pi e^4}{E^2}\left(x\Lambda_{ee} + (1-x)\Lambda_{eH}\right) = \frac{2\pi e^4}{E^2}\Lambda(x+\lambda), \tag{4.1}$$

where e is the electronic charge, Λ_{ee} the electron-electron logarithm for fully ionized media and Λ_{eH} is an effective Coulomb logarithm for electron-hydrogen atom collisions. Numerically $\Lambda_{ee} = 20$ and $\Lambda_{eH} = 7.1$, so $\Lambda = \Lambda_{ee} - \Lambda_{eH} = 12.9$ and $\lambda = \Lambda_{eH}/\Lambda \simeq 0.55$.

Then, in a hydrogen target of ionization level $x(N)$ at column density $N(z)$ the energy loss equation for electron energy E is (cf. equation 2.2)

$$\frac{dE}{dN} = -\frac{2\pi e^4 \Lambda}{E}(\lambda + x(N)) = -\frac{K'}{E}(\lambda + x(N)). \tag{4.2}$$

The energy loss of a given particle with initial energy E_0 depends on the column density $N(z) = \int_0^z n(z')dz'$, so the electron energy at a given distance z from the injection site can be

written $E^2 = E_0^2 - 2K'M(N(z))$ (cf. equation 2.3), where

$$M(N(z)) = \int_0^{N(z)} (\lambda + x(N'))dN' \tag{4.3}$$

is the "effective" ionization-weighted collisional column density.

The atmospheric ionization x as a function of column density N (cm $^{-2}$) changes from 1 to near 0 over a small spatial range in the solar atmosphere. Therefore, to lowest order, $x(N)$ can be approximated by a step function $x(N) = 1$ for $N < N_*$, and $x(N) = 0$ for $N \geq N_*$. This gives $M(N) = (\lambda + 1)N$ for $N < N_*$ and $M(N) = N_* + \lambda N$ for $N \geq N_*$. Electrons injected into the target with energies less than $E_* = \sqrt{2K'(\lambda+1)N_*} = \sqrt{2KN_*}$ experience energy losses and emit X-rays in the fully ionized plasma with $x = 1$, as in the standard thick-target model. Electrons injected with energies higher than E_* lose part of their energy and partially emit X-rays in the un-ionized ($x = 0$), or, more generally, partially ionized plasma.

We can deduce the properties of the X-ray spectrum by substituting Eq. 4.2 into Eq. 2.5 (with $dN = nvdt$) and comparing $I_{thick}(\varepsilon)$ from Eq. 2.4 with $I_{thick}(\varepsilon)$ from Eq. 2.6. We see that for the nonuniformly ionized case the denominator in the inner integral now contains $\lambda + x(N)$ and K is replaced with K'. In the step-function model for $x(N)$, photon energies greater than or equal to $\varepsilon_* = E_*$ are emitted by electrons in the un-ionized plasma with $E \geq E_*$. Since $\lambda + x(N)$ has the constant value λ, the thick-target power-law spectrum is obtained (for in injected power-law spectrum), but the numerical coefficient contains $K'\lambda = 2\pi e^4 \Lambda_{eH}$ instead of K. At photon energies far enough below ε_* that the contribution from electrons with $E \geq E_*$ is negligible, $\lambda + x(N) = \lambda + 1$ and the numerical coefficient contains $(\lambda+1)K' = K$. The usual thick-target spectral shape and numerical coefficient are recovered. The ratio of the amplitude of the high-energy power-law spectrum to the low-energy power-law spectrum is $(\lambda+1)/\lambda \simeq 2.8$. The photon energy $\varepsilon_*(\mathrm{cm}^{-2}) \simeq \sqrt{5.2 \times 10^{-18} \mathrm{N}_*(\mathrm{cm}^{-2})}$, where the photon spectrum flattens below the high-energy power law, determines the value of the column density where the plasma ionization fraction drops from 1 to 0.

4.2 Application to flare X-ray spectra

Kontar et al. (2002, 2003) have fit photon spectra from five flares with the step-function nonuniform ionization model. They assume a single power-law distribution of injected electrons with power-law index δ and approximate the bremsstrahlung cross section with the Kramers cross section. First, they fit the spectra to the sum of a thermal Maxwellian at a single temperature T plus a single power law of index γ. For the 2002 July 23 flare (Kontar et al. 2003) they limit themselves to deviations from a power law in the nonthermal component of the spectrum above ~ 40 keV. The top panel of Figure 4.1 shows an example of such deviations, which represent significant deviations from the power-law fit. These deviations are much reduced by replacing the power law with the spectrum from the nonuniform ionization model, with the minimum rms residuals obtained for values of $\delta = 4.24$ and $E_* = 53$ keV (Figure 4.1, bottom panel). There are still significant residuals present in the range from 10 to 30 keV; these might be due to photospheric albedo or the assumption of a single-temperature thermal component.

By assuming that the main spectral feature observed in a hard X-ray spectrum is due to the increased bremsstrahlung efficiency of the un-ionized chromosphere, allowance for nonuniform target ionization offers an elegant direct explanation for the shape of the observed hard X-ray spectrum and provides a measure of the location of the transition region.

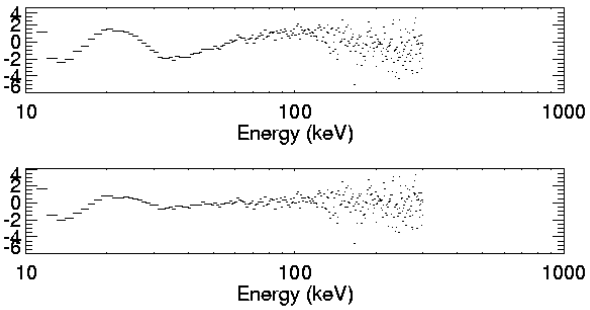

Fig. 4.1 Photon spectrum residuals, normalized by the statistical error for the spectral fit, for the time interval 00:30:00 – 00:30:20 UT 2002-07-23 for (*upper panel*) an isothermal Maxwellian plus a power-law and (*lower panel*) an isothermal Maxwellian plus the nonuniform ionization spectrum with $\delta = 4.24$ and $E_* = 53$ keV (from Kontar et al. 2003)

.

Table 4.1 shows the best fit parameters derived for the four flare spectra analyzed by Kontar et al. (2002). The last column shows the ratio of the minimum χ^2 value obtained from the nonuniform ionization fit to the minimum χ^2 value obtained from a uniform ionization (single power-law) fit to the non-isothermal part of the spectrum. The nonuniform ionization model fits clearly provide substantially better fits than single power-law fits.

Table 4.1 Best fit nonuniformly ionized target model parameters for a single power-law $\mathscr{F}_0(E_0)$, the equivalent N_* (energy range 20-100 keV), and the ratio of $\chi^2_{nonuni}/\chi^2_{uni}$ (from Kontar et al. 2002).

Date	Time, UT	kT(keV)	δ	E_* (keV)	N_* (cm^2)	$\chi^2_{nonuni}/\chi^2_{uni}$
20 Feb 2002	11:06	1.47	5.29	37.4	2.7×10^{20}	0.032
17 Mar 2002	19:27	1.27	4.99	24.4	1.1×10^{20}	0.047
31 May 2002	00:06	2.02	4.15	56.2	6.1×10^{20}	0.041
1 Jun 2002	03:53	1.45	4.46	21.0	8.4×10^{19}	0.055

Kontar et al. (2003) have obtained values of the fit parameters kT (keV), δ and E_* as a function of time for the 2002 July 23 flare, together with the corresponding value of $N_*(\mathrm{cm}^{-2}) \simeq 1.9 \times 10^{17} E_*(\mathrm{keV})^2$. The results (Figure 4.2) demonstrate that the thermal plasma temperature rises quickly to a value $\simeq 3$ keV and decreases fairly slowly thereafter. The injected electron flux spectral index δ follows a general "soft-hard-soft" trend and qualitatively agrees with the time history of the simple best-fit power-law index γ (Holman et al. 2003). E_* rises quickly during the first minute or so from ~ 40 keV to ~ 70 keV near the flare peak and thereafter declines rather slowly. The corresponding values of N_* are $\sim 2 \times 10^{20}$ cm$^{-2} - 5 \times 10^{20}$ cm^{-2}.

The essential results of these studies are that (1) for a single power-law electron injection spectrum, the expression for bremsstrahlung emission from a nonuniformly-ionized target is a better fit to observed spectra than the expression for a uniform target; and (2) the value of E_* (and correspondingly N_*) varies with time.

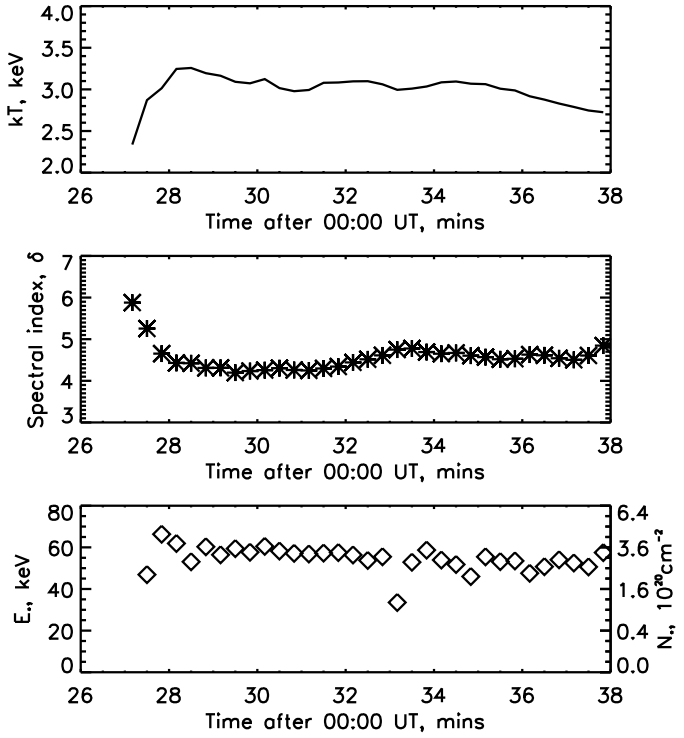

Fig. 4.2 Variation of kT, δ, E_*, and N_* throughout the 2002 July 23 event (Kontar et al. 2003). The variation of other parameters, such as emission measure, can be found in Holman et al. (2003).

5 Return current losses

The thick-target model assumes that a beam of electrons is injected at the top of a loop and "precipitates" downwards in the solar atmosphere. Unless accompanied by positively charged particles, these electrons constitute a current and must create a significant self-induced electric field that in turn drives a return current for compensation (Knight and Sturrock 1977; Emslie 1980; D'Iakonov and Somov 1988). The return current consists of ambient electrons, plus any primary electrons that have scattered back into the upward direction. By this means we have a full electric circuit of precipitating and returning electrons that keeps the whole system neutral, as Ampere's law requires.

The self-induced electric field strength at a given location z along the beam and the flare loop, $\mathscr{E}(z)$, is determined by the current density associated with the electron beam, $j(z)$, and the local conductivity of the loop plasma, $\sigma(z)$: $\mathscr{E}(z) = j(z)/\sigma(z)$. Relating the current density to the density distribution function of the precipitating electrons, $f(z,E,\theta)$, where E is the electron energy and θ is the electron pitch angle, gives

$$\mathscr{E}(z) = \frac{2\sqrt{2}\pi}{\sigma(z)} \frac{e}{\sqrt{m_e}} \int_{-1}^{1} \int_{0}^{\infty} f(z,E,\theta)\sqrt{E}\mu dE d\mu. \quad (5.1)$$

Here μ is the cosine of the pitch angle and e and m_e are the electron charge and mass, respectively. The self-induced electric field strength $\mathscr{E}(z)$ depends on the local distribution of the beam electrons, which in turn depends on the electric field already experienced by the beam as well as any Coulomb energy losses and pitch-angle scattering that may have significantly altered the beam. It also depends on the local plasma density and temperature through $\sigma(z)$, which can in turn be altered by the interaction of the beam with the loop plasma (i.e., "chromospheric evaporation")! Therefore, determination of the self-induced electric field and its impact on the precipitating electrons generally requires self-consistent modeling of the coupled beam/plasma system.

Such models have been computed by Zharkova and Gordovskyy (2005, 2006). They numerically integrate the time-dependent Fokker-Planck equation to obtain the self-induced electric field strength and electron distribution function along a model flare loop. The injected electron beam was assumed to have a single power-law energy spectrum in the energy range from E_{low} = 8 keV to E_{upp} = 384 keV and a normal (Gaussian) distribution in pitch-angle cosine with half-width dispersion $\Delta\mu = 0.2$.

The model computations show that the strength of the self-induced electric field is nearly constant at upper coronal levels and rapidly decreases with depth (column density) in the lower corona and transition region. The rapidity of the decrease depends on the beam flux spectral index. It is steeper for softer beams (δ=5–7) than for harder ones (δ=3). The strength of the electric field is higher for a higher injected beam energy flux density (erg cm $^{-2}$ s^{-1}), and the depth from the injection point over which the electric field strength is highest and nearly constant decreases with increasing beam flux density.

Deceleration of the precipitating beam by the electric field most significantly affects the lower energy electrons ($<$ 100 keV), substantially reducing their number at the upper precipitation depths in the corona where the electric field strength is highest. This leads to flattening of the electron distribution function towards the lower energies and, therefore, flattening of the photon spectrum. In the limit of a constant electric field and no collisional energy losses, this results in a mean electron flux power-law index of $\beta_E = \delta - 1$ and a spectral index of $\gamma = \delta$ for the spatially integrated photon spectrum.

Photon spectra computed from kinetic solutions that include return current energy losses and collisional energy losses and scattering are shown in Fig. 5.1 (a) and (b). Low- and high-energy spectral indices and their dependence on the power-law index of the injected electron distribution and on the injected beam energy flux density are shown in Fig. 5.1 (c) and (d). The difference between the high and low spectral indices is seen to increase with both the beam energy flux density and the injected electron power-law index δ. The low index is found to be less than 2 for δ as high as 5 when the energy flux density is as high as 10 ^{12} erg cm^{-2} s^{-1}.

We have seen that return current energy losses can introduce curvature into a spectrum, possibly explaining the "break" often seen in observed flare X-ray spectra. A difficulty in directly testing this explanation is that the thick-target model provides the power (energy flux) in the electron beam (erg s^{-1}), but not the energy flux density (erg cm^{-2} s^{-1}). X-ray images provide information about the area of the target, but this is typically an upper limit on the area. Even if the source area does appear to be well determined, the electron beam can be filamented so that it does not fill the entire area (the filling factor is less than 1). Therefore, the observations typically only give a lower limit on the beam energy flux density.

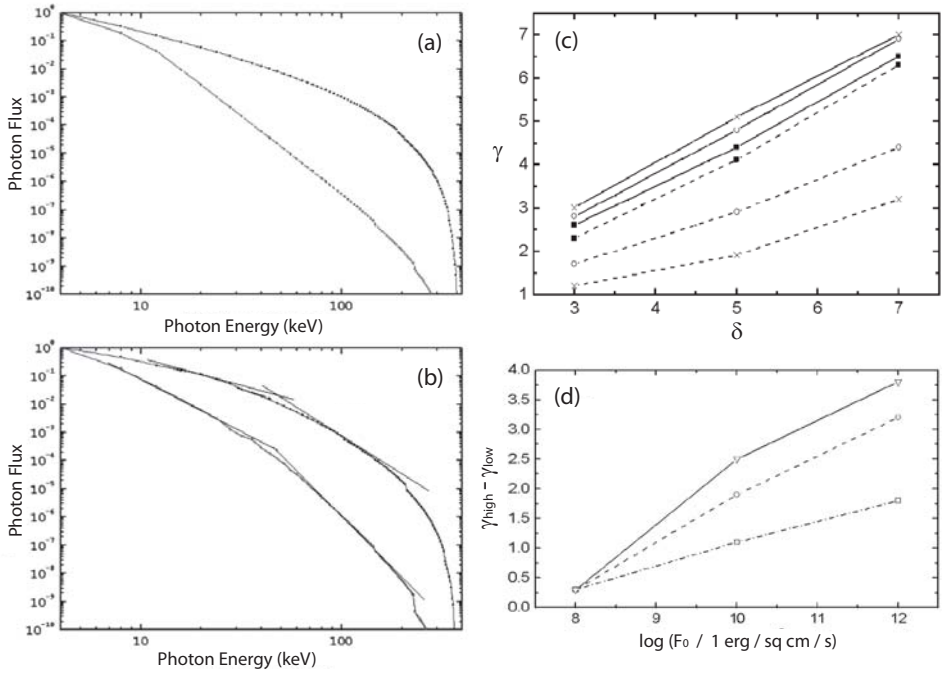

Fig. 5.1 (a) Photon spectra computed from full kinetic solutions including return current losses and collisional losses and scattering. The top spectrum is for an injected electron flux power-law index of $\delta = 3$, and the bottom spectrum is for $\delta = 7$. The injected electron energy flux density is 10^{8} erg cm^{-2} s^{-1}. (b) Same as (a), but for an injected energy flux density of 10^{12} erg cm^{-2} s^{-1}. The tangent lines demonstrate the determination of the lower and upper power-law spectral indices γ_{low} and γ_{high}. (c) The photon spectral indices γ_{low} (dashed lines) and γ_{high} (solid lines) vs. δ for an injected energy flux density of 10^{8} (squares), 10^{10} (circles), and 10^{12} erg cm^{-2} s^{-1} (crosses). (d) $\gamma_{high} - \gamma_{low}$ vs. the log of the injected electron energy flux density for δ equal to 3 (bottom curve, squares), 5 (middle curve, circles), and 7 (top curve, triangles). (from Zharkova and Gordovskyy 2006).

Alexander and Daou (2007) have deduced the photon flux from nonthermal electrons in a sample of 10 flares ranging from GOES class M1.8 to X17. They find that the nonthermal photon flux does not monotonically increase with the thermal energy flux, but levels off (saturates) as the thermal energy flux becomes high. They argue that this saturation most likely results from the growing importance of return current energy losses as the electron beam flux increases to high values in the larger flares.

Sui et al. (2007) found a correlation between the X-ray flux and spectral break energy in early impulsive flares (see Section 3.5). They point out that the increasing significance of return current energy losses at higher electron energies as the electron beam energy flux density increases could be an explanation for this correlation.

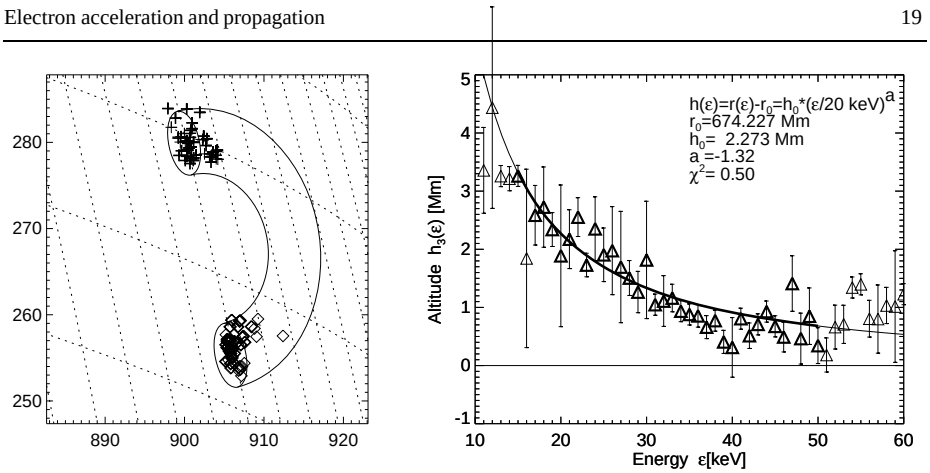

Fig. 6.1 The centroids of footpoint hard X-ray emission are marked for different photon energies between 10 keV and 60 keV for the 2002 February 20, 11:06 UT, flare, which occurred near the solar west limb and was imaged with RHESSI (left panel). The altitude $h(\varepsilon)$ as a function of energy ε shows a systematic height decrease with increasing energy (right panel) (from Aschwanden et al. 2002).

6 Height dependence and size of X-ray sources with energy and time

6.1 Footpoint Sources

Hard X-ray footpoint sources result from collisional bremsstrahlung of precipitating electrons, which produce most of the emission in the chromosphere according to the thick-target model. Essentially, mildly energetic electrons lose their energy in the lower corona or transition region, while the more energetic electrons penetrate deeper into the chromosphere (see equation 2.2).

The altitude of these hard X-ray footpoint sources could never be measured accurately before RHESSI, because of a lack of spatial and spectral resolution. With RHESSI we can measure the centroid of the footpoint location within an accuracy of order an arcsecond for every photon energy in steps as small as 1 keV. For a flare near the limb (Fig. 6.1), the centroid location translates directly into an altitude.

Aschwanden et al. (2002) studied such a flare observed on 2002 February 20, where the heights of the footpoint sources were fitted with an exponential function of the photon energy, which yielded altitudes in the range of $h \approx 1000 - 5000$ km in the energy range of $\varepsilon = 10 - 60$ keV, progressively lower with higher energy, as expected from the thick-target model (Fig. 6.1, right frame).

Since the stopping depth of the precipitating electrons is a function of column density, the integrated density along their path in the chromosphere (Brown et al. 2002), the measured height dependence of the hard X-ray centroids can be inverted to yield a density model of the chromosphere. The inversion of the RHESSI data in the example shown in Fig. 6.1 yielded a chromospheric density model that has a significantly higher electron density in the $h = 2000 - 5000$ km range than the standard chromospheric models based on UV spectroscopy and hydrostatic equilibrium (VAL and FAL models). The RHESSI-based chromospheric density model is therefore more consistent with the "spicular extended chromosphere", similar to the results from sub-mm radio observations during solar eclipses carried out at Caltech (Ewell et al. 1993).

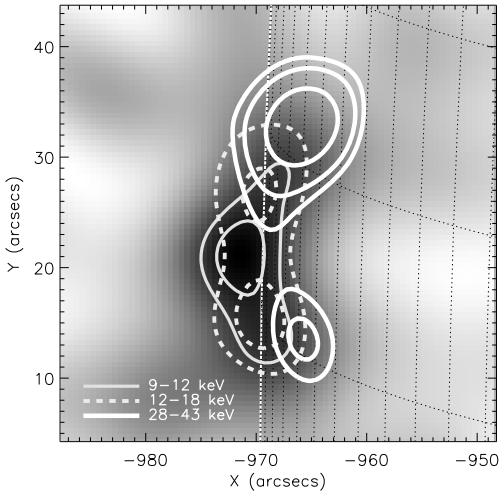

Fig. 6.2 CLEAN images at 04:58:22–04:58:26 UT during the impulsive phase of the 2003 November 13 M1.7 flare. The background shows the image at 9-12 keV. The contour levels are 75% and 90% of the peak flux at 9–12 keV (*looptop*), 70% and 90% at 12–18 keV (*legs*), and 50%, 60%, & 80% at 28–43 keV (*footpoints*) (from Liu et al. 2006).

6.2 Loop Sources and their Evolution

As discussed above, footpoint sources are produced by bremsstrahlung emission in the thick-target chromosphere. The compactness of such sources results from the rapid increase of the atmosphere density from the tenuous corona to the dense chromosphere. This also gives rise to the compact height distribution of emission centroids at different energies as shown in the 2002 February 20 flare above reported by Aschwanden et al. (2002). However, if the density distribution has a somewhat gradual variation, one would expect a more diffuse height distribution. Specifically, at some intermediate energies, we expect that HXR emission would appear at the legs of the loop, rather than the commonly observed looptop sources at low energies or footpoint sources at high energies. This is exactly what *RHESSI* has observed, for the first time, in an M1.7 flare (Liu et al. 2006) occurring on 2003 November 13 (Figure 6.2) and in a C1.1 flare on 2002 November 28 (Sui et al. 2006).

To reveal more details of the energy-dependent structure of the 2003 November 13 event, Figures 6.3*a*-6.3*c* show the X-ray emission profile along the flare loop at different energies for three time intervals in sequence. The high energy emission is dominated by the footpoints, but there is a decrease of the separation of the footpoints with decreasing energies and with time. At later times the profile becomes a single source, peaking at the looptop. The general trend suggests an increase of the plasma density in the loop with time (Liu et al. 2006), which can be produced by chromospheric evaporation and can give rise to progressively shorter stopping distances for electrons at a given energy. Such a density increase also smoothes out to some extent the sharp density jump at the transition region. This results in

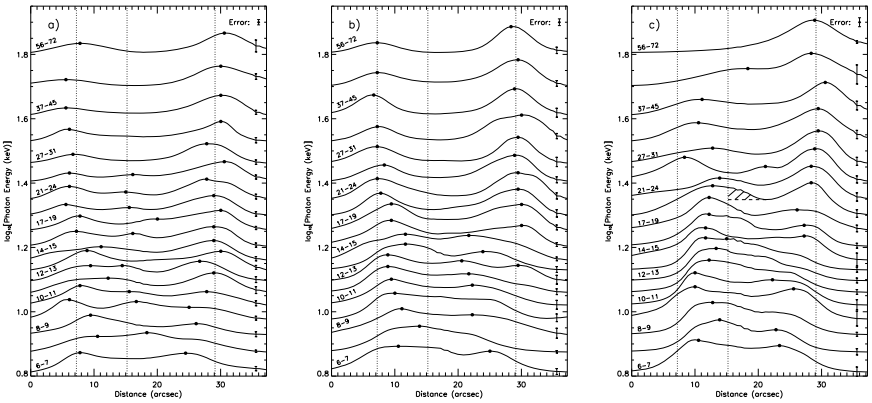

Fig. 6.3 (*a*) Brightness profiles along the flaring loop at different energies for the time interval 04:58:00–04:58:24 UT on November 13, 2003. The vertical axis indicates the average photon energy (logarithmic scale) of the energy band for the profile. Representative energy bands (in units of keV) are labeled above the corresponding profiles. The filled circles mark the local maxima, and the vertical dotted lines are the average positions of the centroids of the looptop and footpoint sources. (*b, c*) Same as (*a*), but for 04:58:24–04:58:48 and 04:58:48–04:59:12 UT, respectively. The error bars show the uncertainty of the corresponding profile (from Liu et al. 2006).

the nonthermal bremsstrahlung HXRs at intermediate energies appearing in the legs of the loop, at higher altitudes than the footpoints, as shown in Figure 6.2.

From the emission profiles in the nonthermal regimes of the photon spectra, Liu et al. (2006) derived the density distribution along the loop, using the empirical formula for nonthermal bremsstrahlung emission profiles given by Leach and Petrosian (1983, Eq. 11). This way, one does not need to pre-assume any model form of the density distribution (cf., Aschwanden et al. 2002). Figure 6.4 shows the density profiles derived from the emission profiles in the three time intervals shown in Figure 6.4. Between the first and second intervals, the density increases dramatically in the lower part of the loop, while the density near the looptop remains essentially unchanged. The density enhancement then shifts to the looptop from the second to the third interval. This indicates a mass flow from the chromosphere to the looptop, most likely caused by chromospheric evaporation. For papers studying chromospheric evaporation using coordinated *RHESSI* HXR and EUV Doppler shift observations, see Milligan et al. (2006a,b) and Brosius and Holman (2007).

The 2002 November 28 flare was an early impulsive flare, meaning that pre-heating of plasma to X-ray-emitting temperatures was minimal. Early impulsive flares are identified in practice by searching for flares for which the $>$25 keV hard X-ray flux increase is delayed by less than 30 s after the flux increase at lower energies (Sui et al. 2006, 2007). These flares provide the opportunity to observe the X-ray emission from nonthermal electrons to lower energies than would otherwise be possible.

RHESSI observations of this flare showed coronal X-ray sources that first moved downward and then upward along the legs of the flare loop (Sui et al. 2006). The bottom panel of Figure 6.5 shows the motion of the sources observed in the 3–6 keV band. RHESSI and GOES light curves are shown in the top panel for comparison. The sources originated at the top of the flare loop and then moved downward along both legs of the loop until the time of peak emission at energies above 12 keV. Afterward the source in the northern leg

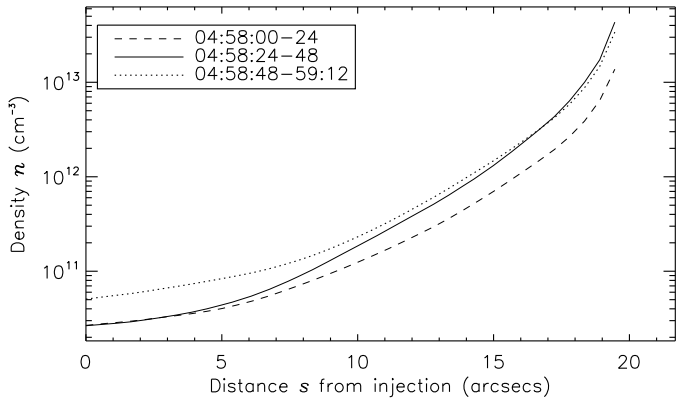

Fig. 6.4 Averaged density profiles along the loop inferred from the HXR brightness profiles during the three time intervals in Fig. 6.3. The distance is measured from the top of the loop (from Liu et al. 2006).

of the loop was no longer observable, but the source in the southern leg moved back to the top of the loop. Its centroid location at the looptop was slightly but significantly lower than the centroid position at the beginning of the flare. Higher energy sources showed a similar evolution, but higher energy sources had lower centroid positions.

The early downward source motion along the legs of the loop is a rare, previously unobserved phenomenon. At this time we do not know if the occurrence is rare, or if it is simply rarely observed because of masking by the radiation from the thermal plasma. Sui et al. (2006) argue that the motion results from the hardening of the X-ray spectrum, and possibly an increase in the low-energy cutoff, as the flare hard X-ray emission rises to its peak intensity. A flatter spectrum results in a higher mean energy of the electrons contributing to the radiation at a given X-ray energy. In a loop with a plasma density that increases significantly from the top to the footpoints, these higher energy electrons will propagate to a lower altitude in the loop as the spectrum hardens. The softening of the spectrum after peak emission would also contribute to the upward motion of the source after the peak. However, at this time chromospheric evaporation is likely to be increasing the density in the loop, as discussed above for the 2003 November 13 flare, and thermal emission is becoming more important. All of these can contribute to an increase in the height of the centroid of the X-ray source. The downward motion may only occur in initially cool flare loops, i.e., early impulsive flares, because these loops are most likely to contain the density gradients that are required.

Xu et al. (2008) modeled the size dependence with photon energy of coronal X-ray sources observed by RHESSI in ten M-class limb flares. They determined the one-sigma Gaussian width of the sources along the length of the flare loops by obtaining forward fits to the source visibilities. The integration times ranged from one to ten minutes and the source sizes were determined in up to eight energy bins ranging in energy from as low as 7 keV to as high as 30 keV. They found the source sizes to increase slowly with photon energy, on average as $\varepsilon^{1/2}$.

The results were compared with several models for the variation of the source size with energy. The source size was shown to vary as $\varepsilon^{-1/2}$ for a thermal model with a constant loop density and a temperature that decreased with a Gaussian profile along the legs of the

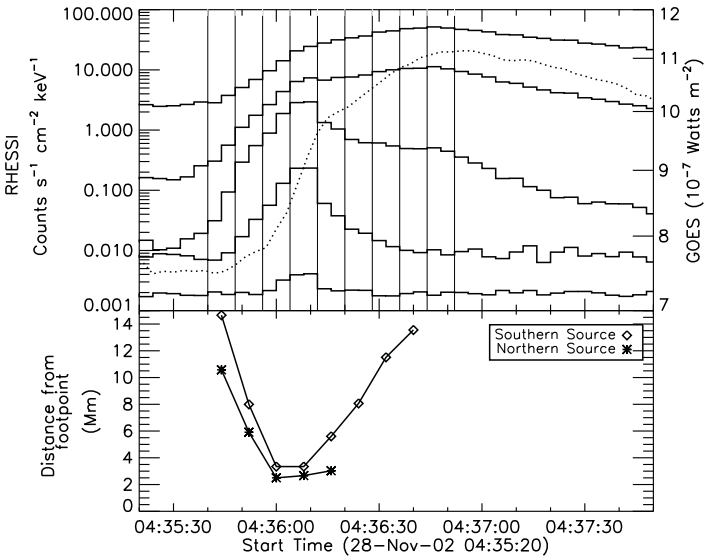

Fig. 6.5 RHESSI (*solid lines*) and GOES 1–8 Å(*dotted line*) light curves are shown in the *top panel*. The RHESSI energy bands (from top to bottom) are 3–6, 6–12, 12–25, and 50–100 keV, with scaling factors of 5, 1, 4, 3, and 0.5, respectively. The RHESSI and GOES integration times are 4 and 3 s, respectively. The *bottom panel* shows the distance between the 3–6 keV moving source centroids and their corresponding footpoint centroids located in the 25–50 keV image of the flare at the time of peak emission. The distances are plane-of-sky values with no correction for motions away from or toward the observer (from Sui et al. 2006).

loop from a maximum temperature at the top of the loop. For the injection of a power-law electron flux distribution into a high-density loop so that the loop is a collisional thick target, the source size was shown to increase as ε^2. Neither of these models are consistent with the $\varepsilon^{1/2}$ dependence. A hybrid thermal/nonthermal model and a nonthermal model with an extended acceleration region were found to be consistent with the deduced scaling, however. The extended acceleration region was found to have a half-length in the range $10\ ''-18''$ and density in the range $(1-5)\times 10^{11}$ cm^{-3}.

7 Hard X-ray timing

The analysis of energy-dependent time delays allows us to test theoretical models of physical time scales and their scaling laws with energy. In the wavelength domain of hard X-rays there are at least three physical processes known in the observation of solar flares that lead to measurable time delays as a function of energy (for a review, see Aschwanden 2004): (1) time-of-flight dispersion of free-streaming electrons, (2) magnetic trapping with the collisional precipitation of electrons, and (3) cooling of the thermal plasma.

7.1 Time-of-Flight Delays

The first type, the *time-of-flight (TOF)* delay, has a scaling of $\Delta t(\varepsilon) \propto \varepsilon^{-1/2}$ and are caused by velocity differences of electrons that propagate from the coronal acceleration site to the chromospheric energy-loss region, observable as time differences of order $\Delta t \approx 10 - 100$ ms for nonthermal electrons at energies $E \approx 20 - 100$ keV (e.g., Aschwanden et al. 1995, 1996). The measurement of such tiny time delays requires high photon statistics and high time resolution, which was most suitably studied with the *Compton Gamma Ray Observatory (CGRO).* This has been much harder to accomplish with RHESSI, in particular because we are not yet able to adequately subtract out the rotational modulation (caused by the spinning spacecraft) in the time profiles.

These studies of TOF delays have provided important evidence that electrons are accelerated in the corona, above the top of the hot flare loops observed in soft X-rays. The fine structure in the light curves of most, but not all, of the studied flares showed energy-dependent time delays consistent with the free streaming of electrons to the footpoints of the flare loops from an origin somewhat more distant than the half-length of the loops (Aschwanden et al. 1995; Aschwanden and Schwartz 1995; Aschwanden et al. 1996).

7.2 Trapping Delays

The second type, the *trapping delay*, is caused by magnetic mirroring of coronal electrons which precipitate toward the chromosphere after a collisional time scale, which has the scaling of $\Delta t(\varepsilon) \propto \varepsilon^{3/2}$ and is observable from time differences of $\Delta t \approx 1 - 10$ s for nonthermal electrons at $E \approx 20 - 100$ keV (e.g., Vilmer et al. 1982; Aschwanden et al. 1997). Such trapping delays could potentially be studied with RHESSI, if cleanly demodulated time profiles can be obtained.

Aschwanden et al. (1997) found time delays in the gradually varying component of CGRO flare HXR light curves to be consistent with magnetic trapping and collisional precipitation of the particles. Trap plasma densities $\sim 10^{11}$ cm^{-3} were deduced. No evidence was found for second-step acceleration of electrons with energies ≤ 200 keV.

7.3 Thermal Delays

The third type, the *thermal delay*, can be caused by the temperature dependence of cooling processes, such as by thermal conduction, $\tau_c(T) \propto T^{-5/2}$ (e.g., Antiochos and Sturrock 1978; Culhane et al. 1994), or by radiative cooling, $\tau_r(T) \propto T^{5/3}$ (e.g., Fisher and Hawley 1990; Cargill et al. 1995). The observed physical parameters suggest that thermal conduction dominates in flare loops at high temperatures as observed in soft X-ray wavelengths, while radiative cooling dominates in the later phase of cooling in postflare loops as observed in EUV wavelengths (Antiochos and Sturrock 1978; Culhane et al. 1994; Aschwanden and Alexander 2001). When the temperature drops ($dT(t)/dt < 0$) in the decay phase of flares, the heating rate can justifiably be neglected and the conductive or radiative cooling rate dominate the temperature evolution. Before RHESSI, the cooling curve $T(t)$ in flare plasmas had been studied in only a few flares (e.g., Culhane et al. 1994; Aschwanden and Alexander 2001).

The high spectral resolution of RHESSI data is particularly suitable for any type of thermal modeling, because we can probe the thermal plasma from ≈ 3 keV up to ≈ 30 keV

with a resolution of $\gtrsim$1 keV thanks to the cooled germanium detectors (Lin et al. 2002). This allows us to measure flare temperatures with more confidence, and a statistical study of flare temperatures measured in the range of $T \approx 7-20$ MK indeed demonstrates some agreement between the values obtained from spectral fitting of RHESSI data with those obtained from flux ratios with GOES (Battaglia et al. 2005), although RHESSI has a bias for the high-temperature tail of the differential emission measure (DEM) distribution (Aschwanden, Stern, & Güdel 2007; Väänänen & Pohjolainen 2007) . Of course, we expect an agreement between the emission-measure-weighted temperatures (which roughly correspond to the peak of the DEMs) only when both instruments are sensitive in a temperature range that covers the flare DEM peak.

A close relationship between the nonthermal and thermal time profiles was found early on, in the sense that the thermal emission often closely resembles the integral of the nonthermal emission, a relationship that is now known as the *Neupert effect* (Hudson 1991; Dennis and Zarro 1993). This relationship is, however, strictly only expected for the asymptotic limit of very long cooling times, while a physically more accurate model would quantify this effect by a convolution of the nonthermal heating with a finite cooling time. The deconvolution of the e-folding cooling time in such a model has never been attempted statistically and as a function of energy or temperature. The cooling time at a given energy can be estimated from the decay time of a flare time profile. For instance, the decay times measured with GOES in soft X-rays were found to have a median of $\tau_{decay} \approx 6$ min (Veronig et al. 2002b,a). The Neupert effect was tested by correlating the soft X-ray peak flux with the (time-integrated) hard X-ray fluence. A high correlation and time coincidence between the soft X-ray peak and hard X-ray end time was generally found, but a significant fraction of events also had a different timing (Veronig et al. 2002c). Tests of the "theoretical Neupert effect", i.e., comparisons of the beam power supply of hard X-ray-emitting electrons and the thermal energy of evaporated plasma observed in soft X-rays, found it to strongly depend on the low-energy cutoff to the nonthermal electron distribution (Veronig et al. 2005).

7.4 Multi-Thermal Delay Modeling with RHESSI

Since major solar flares generally produce a large number of individual postflare loops, giving the familiar appearance of loop arcades lined up along the flare ribbons, it is unavoidable that each loop is heated and cools off at different times, so that a spatially integrated spectrum always contains a multi-thermal differential emission measure distribution. The resulting multi-thermal bremsstrahlung spectrum (for photon energies ε) observed in soft X-rays (neglecting the Gaunt factor of order unity),

$$F(\varepsilon) = F_0 \int \frac{\exp(-\varepsilon/k_B T)}{T^{1/2}} \frac{dEM(T)}{dT} dT \ , \tag{7.1}$$

is then a function of a multi-thermal *differential emission measure* distribution $dEM(T) = n^2(T)dV$. An example of a multi-thermal spectrum from a differential emission measure proportional to T^{-4} up to a maximum temperature of 50 MK is shown in Fig. 7.1.

The initial cooling of the hot flare plasma (say at $T \gtrsim 10$ MK) is generally dominated by conductive cooling (rather than by radiative cooling, which can dominate later after the plasma cools to EUV-emitting temperatures of $T \lesssim 2$ MK). The thermal conduction time has the following temperature dependence:

$$\tau_{cond}(T) = \frac{\varepsilon_{th}}{dE/dt_{cond}} = \frac{3 n_e k_B T}{\frac{d}{ds}\kappa T^{5/2}\frac{dT}{ds}} \approx \frac{21}{2}\frac{n_e L^2 k_B}{\kappa} T^{-5/2} = \tau_{c0}\left(\frac{T}{T_0}\right)^{-5/2} . \tag{7.2}$$

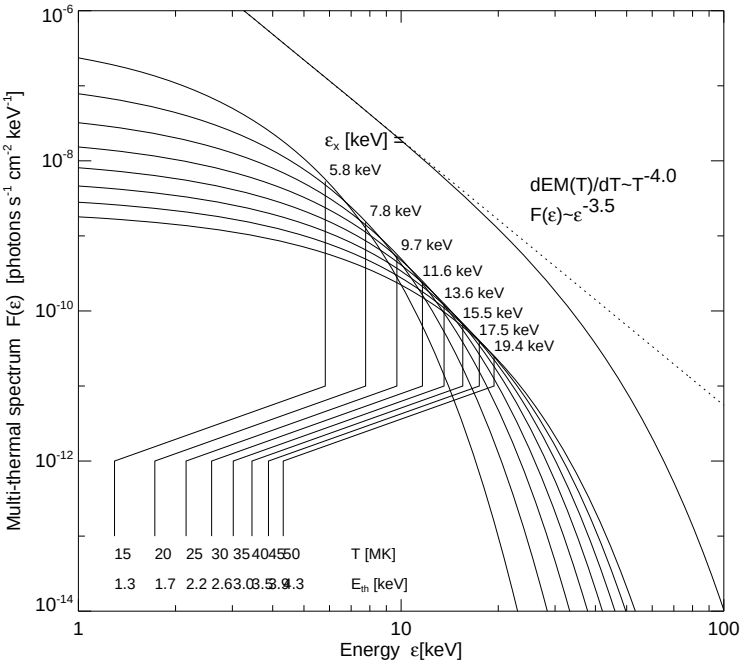

Fig. 7.1 Example of a multi-thermal spectrum with contributions from plasmas with temperatures of $T = 15, 20, ..., 50$ MK and a DEM distribution of $dEM(T)/dT \propto T^{-4}$. The individual thermal spectra and their sum are shown with thin linestyle, where the sum represents the observed spectrum. Note that the photons in the energy range $\varepsilon = 5.8 - 19.4$ keV are dominated by temperatures of T=15–50 MK, which have a corresponding thermal energy that is about a factor of $(\delta + 1/2) = 4.5$ lower ($\varepsilon_{th} = 1.3 - 4.3$ keV). The photon spectrum without the high-energy cutoff approaches the power-law function $F(\varepsilon) \propto \varepsilon^{-3.5}$ (from Aschwanden 2007).

Since the thermal bremsstrahlung at increasing photon energy is dominated by radiation from higher temperature flare plasma, the conductive cooling time is expected to become shorter with higher temperatures ($\tau_{cond} \propto T^{-5/2}$), or vice versa, longer cooling delays are expected at lower energies. Thus, the soft X-ray peak is always delayed with respect to the harder X-ray peaks, reflecting the cooling of the flare loops.

Aschwanden (2007) has measured and modeled this conductive cooling delay $\tau_{cond}(\varepsilon)$ for a comprehensive set of short-duration (≤ 10 min) flares observed by RHESSI. One example is shown in Fig. 7.2. He finds that the cooling delay Δt expressed as a function of the photon energy ε and photon spectral index γ can be approximated by

$$\Delta t(\varepsilon, \gamma) \approx \tau_g \frac{7}{4} \left[\log \left(1 + \frac{\tau_{c0}}{\tau_g} \left(\frac{\varepsilon}{(\gamma - 1)\varepsilon_0} \right)^{-\beta} \right) \right]^{3/4} , \qquad (7.3)$$

(where τ_g is the Gaussian width of the time profile peak) and yields a new diagnostic of the process of conductive cooling in multi-thermal flare plasmas. In a statistical study of 65 flare events (Aschwanden 2007), 44 (68%) were well fit by the multi-thermal model with a best fit value for the exponent of $\beta = 2.7 \pm 1.2$, which is consistent with the theoretically expected

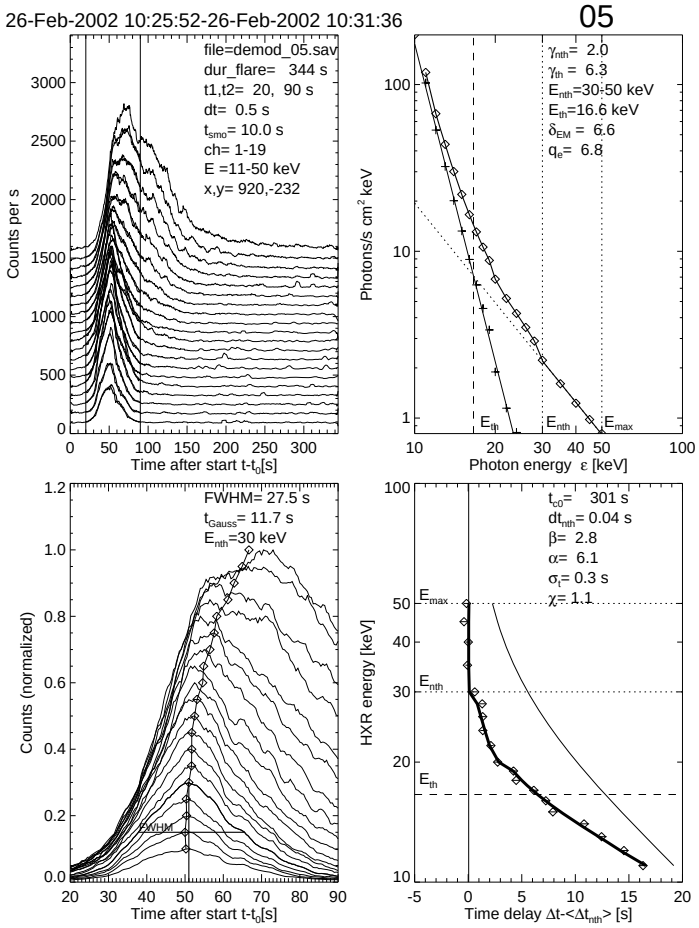

Fig. 7.2 X-ray light curves are shown for the 2002 February 26, 10:31 UT, flare, for energies of 10 keV to 30 keV in intervals of 1 keV, observed with RHESSI (left panels). The spectrum is decomposed into thermal and nonthermal components (top right panel) and the delay of the peaks at different energies is fitted with a thermal conduction cooling time model that has a scaling of $\tau_{cond}(T) \approx T^{-\beta}$ (right bottom panel). The best fit shows a power index of $\beta = 2.8$, which is close to the theoretically expected value of $\beta = 5/2$ (Eq. 7.2). The full delay of the thermal component is indicated with a thin curve (bottom left panel), while the weighted (thermal+nonthermal) fit is indicated with a thick curve (from Aschwanden 2007).

value of $\beta = 2.5$ according to Eq. 7.2. The conductive cooling time at $T_0 = 11.6$ MK ($\varepsilon_0 = 1$ keV) was found to range from 2 to 750 s, with a mean value of $\tau_{c0} = 40$ s.

8 Hard X-ray spectral evolution in flares

8.1 Observations of spectral evolution

The nonthermal hard X-ray emission from solar flares, best observed in the 20 to 100 keV range, is highly variable. Often several emission spikes with durations ranging from seconds to minutes are observed. In larger events, sometimes a more slowly variable, long duration

emission can be observed in the later phase of the flare. Hence, most flares seems to start out with an *impulsive* phase, while some events, mostly large ones, show the presence of a late *gradual* phase.

While these two different behaviors can already be spotted by looking at lightcurves, they also are distinct in their spectral evolution. The impulsive spikes tend to be harder at peak time, and softer both in the rise and decay phase. The spectrum starts soft, gets harder as the flux rises and softens again after the maximum of the emission. This pattern of the spectral evolution is thus called *soft-hard-soft* (SHS). On the other hand, in the gradual phase, the flux slowly decreases, while the spectrum stays hard or gets even harder. This different kind of spectral evolution is called *soft-hard-harder* (SHH).

Historically, both the SHS (Parks and Winckler 1969; Kane and Anderson 1970) and the SHH behavior (Frost and Dennis 1971) were observed in the early era of hard X-ray observations of the Sun. Subsequent investigation confirmed both the SHS (Benz 1977; Brown and Loran 1985; Lin and Schwartz 1987; Gan 1998; Fletcher and Hudson 2002; Hudson and Fárník 2002) and the SHH (Frost and Dennis 1971; Cliver et al. 1986; Kiplinger 1995) patterns.

While all these observations established the qualitative properties of the spectral evolution, a statistical analysis of the quantitative relation between the flux and spectral index had not been performed in the pre-RHESSI era. Here, we summarize RHESSI results investigating quantitatively the spectral evolution of the non-thermal component of the hard X-ray emission, as well as the theoretical implications. More details can be found in Grigis and Benz (2004, 2005, 2006).

To quantify the spectral evolution, a simple parameterization for the shape of the non-thermal spectrum is needed. Luckily, in solar flares the spectrum is well described by a power-law in energy, which often bends downward above 50 keV. Such a softening of the spectrum can be modeled by a broken power-law model. However, it is difficult to observe such a downward bending at times of weak flux, because the high-energy region of the spectrum is lost in the background. As a compromise, a single power-law was fitted to the data at all times. Although the single power law does not always provide a good fit to the spectra, it provides a characteristic spectral slope and ensures an equal treatment of the spectra at different times.

The two free parameters of the power-law model are the spectral index γ and the power-law normalization F_{ε_0} at the reference energy ε_0. The reference energy ε_0 is arbitrary, but fixed. The time dependent spectrum is given by

$$I(\varepsilon,t) = I_{\varepsilon_0}(t)\left(\frac{\varepsilon}{\varepsilon_0}\right)^{-\gamma(t)}. \tag{8.1}$$

A representative sample of 24 solar flares of GOES size between M1 and X1 was selected, and the spectral model (Eq. 8.1), with the addition of an isothermal emission component at low energies, was fitted with a cadence of one RHESSI spin period (about 4 seconds). This delivered a sequence of measurements of the quantities $I_{\varepsilon_0}(t)$ and $\gamma(t)$ for each of the 24 events, covering a total span of about 62 minutes of non-thermal hard X-ray emission. For these events, $\varepsilon_0 = 35$ keV was chosen, a meaningful energy which lies about in the middle of the range where the nonthermal emission is best observed in these M-class flares.

An example of the measured time evolution of the spectral index γ and the flux normalization I_{35} for the longer-lasting event of the set is shown in Fig. 8.1. We note that I_{ε_0} changes more strongly than γ; therefore, we plot the flux normalization on a logarithmic scale.

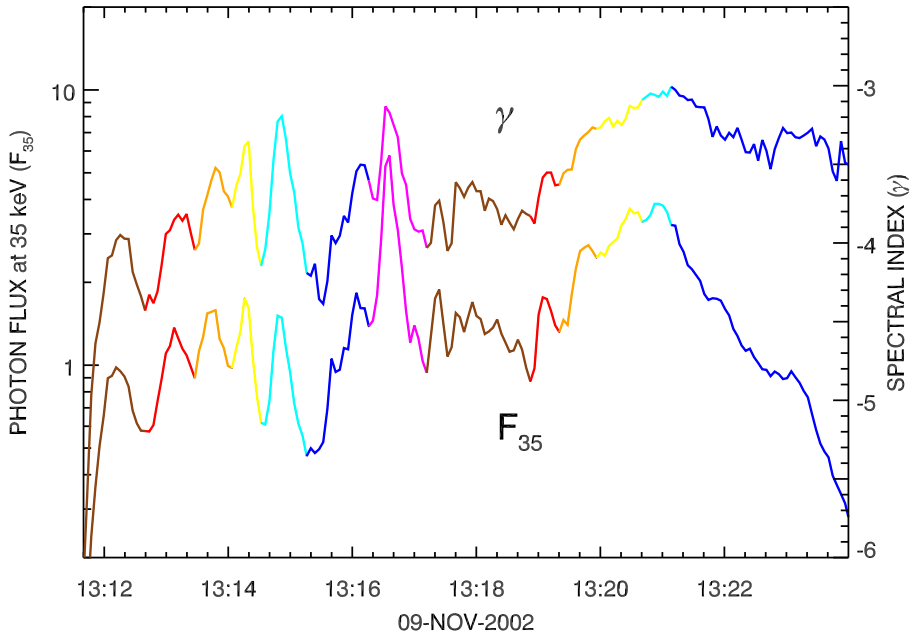

Fig. 8.1 Time evolution of the spectral index $-\gamma$ (*upper curve, linear scale on right*) and the flux normalization I_{35}(*lower curve, logarithmic scale on left*) of the nonthermal component in the flare of November 9, 2002. Different emission spikes are shown in different colors (after Grigis and Benz 2004).

A correlation in time between the two curves can be readily seen. Single emission spikes are plotted in different colors, so that the soft-hard-soft evolution can be observed not only as a general trend, but also during each spike (with the exception of the late, more gradual phase, where the emission stays hard as the flux decays).

As there is an anti-correlation in time between $\log I_{35}(t)$ and $\gamma(t)$, a plot of one parameter as a function of the other, eliminating the time dependence, shows the relationship between them. Figure 8.2 shows plots of γ vs. I_{35} for 3 events where there are only one or two emission peaks. The points in the longer uninterrupted rise or decay phase during each event are marked by plus symbols. A linear relationship between $\log I_{35}$ and γ can be seen during each phase, although it can be different during rise and decay.

On the other hand, a plot of all the 911 fitted model parameters for all the events show a large scatter, as shown in Fig. 8.3. The large scatter can be understood as originating from the superposition of data from a large numbers of different emission spikes, each featuring linear trends with different parameters. This plot does demonstrate, however, the tendency for flatter spectra to be associated with higher intensity flares.

8.2 Interpretation of spectral evolution

Can we explain the soft-hard-soft spectral behavior theoretically? The problem here is that many effects concur in the production of the high-energy electrons whose bremsstrahlung

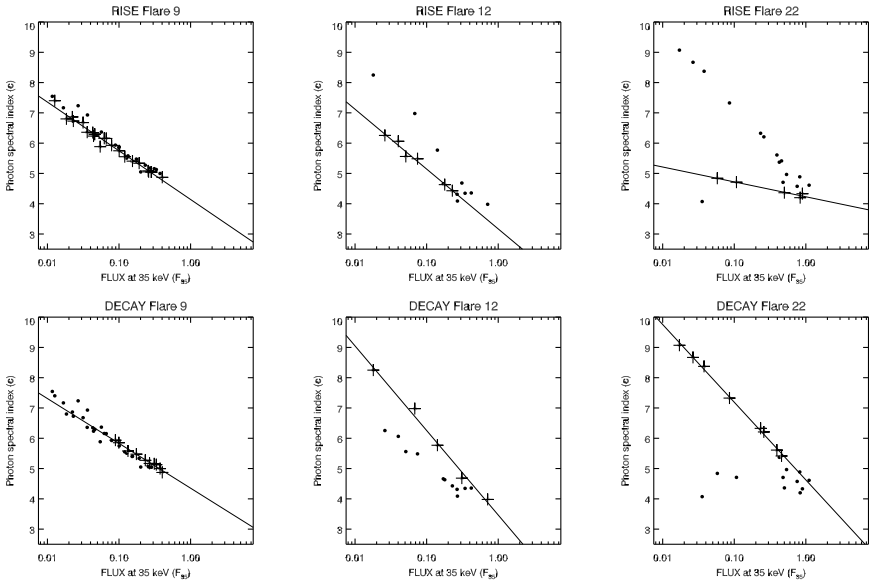

Fig. 8.2 Spectral index γ vs. flux normalization I_{35} for three events, showing the linear dependence of single rise and decay phases of emission spikes on a log-linear scale. Dots mark results from individual spikes, while pluses mark the longer rise or decay phase (from Grigis and Benz 2004).

hard X-ray are observed by RHESSI and similar instruments. We can identify three main, closely related physical mechanisms which are responsible for the production of these energetic particles: the *acceleration* of part of the thermal ambient plasma, the *escape* from the acceleration region and the *transport* to the emitting region.

Miller et al. (1996), hereafter MLM, proposed a stochastic acceleration mechanism where electrons are energized by small amplitude turbulent fast-mode waves, the transit-time damping model. MLM showed that their model could successfully account for the observed number and energy of electrons accelerated above 20 keV in subsecond spikes or energy release fragments in impulsive solar flares. However, they made no attempt to explain the observed hard X-ray spectra (which are softer than predicted by the transit-time damping model) and did not consider spectral evolution. The MLM approach does not account for escape. Grigis and Benz (2006) extend the MLM model with the addition of a term describing the escape of the accelerated particles from the accelerator. To ensure conservation of particles, they also add a source term of cold particles coming into the accelerator (such as can be provided by a return current).

The stochastic nature of this acceleration model implies that the electrons undergo a diffusion process in energy space. Mathematically, the acceleration is described by the following convective-diffusive equation:

$$\frac{\partial f}{\partial t} = \frac{1}{2}\frac{\partial^2}{\partial E^2}\Big[(D_{\rm COLL} + D_{\rm T})\, f\Big] - \frac{\partial}{\partial E}\Big[(A_{\rm COLL} + A_{\rm T})\, f\Big] - S(E)\cdot f + Q(E)\,, \qquad (8.2)$$

where $f(E)$ is the electron density distribution function, $D_{\rm T}$ and $A_{\rm T}$ are, respectively, the diffusion and convection coefficients due to the interactions of the electrons with the accelerating turbulent waves, $D_{\rm COLL}$ and $A_{\rm COLL}$ are, respectively, the diffusion and convection coefficients due to collisions with the ambient plasma, $S(E)$ is the sink (escape) term,

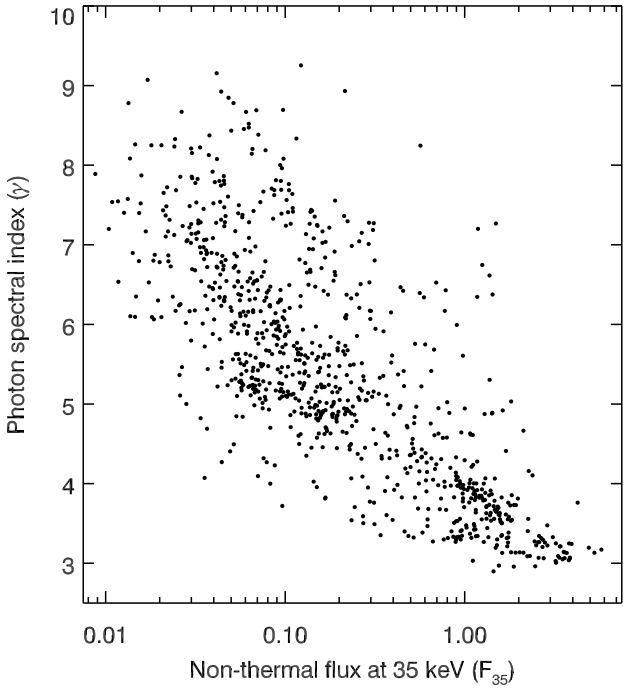

Fig. 8.3 Plot of the spectral index γ versus the fitted nonthermal flux at 35 keV (given in photons s $^{-1}$ cm^{-2} keV^{-1}). All 911 data points from the 24 events are shown (from Grigis and Benz 2004).

and $Q(E)$ is the source (return current) term. The escape term is proportional to $v(E)/\tau$, where $v(E)$ is the electron speed, and τ is the escape time. The escape time can be energy-dependent, but for simplicity we keep it constant at first. The longer the escape time is, the better the particles are trapped in the accelerator. The source term is in the form of a Maxwellian distribution of electrons with the same temperature as the ambient plasma.

The coefficients $D_{\rm T}$ and $A_{\rm T}$ are proportional to the dimensionless acceleration parameter

$$I_{\rm ACC} = \frac{U_{\rm T}}{U_{\rm B}} \cdot \frac{c\langle k\rangle}{\Omega_{\rm H}}, \tag{8.3}$$

where $U_{\rm T}$ and $U_{\rm B}$ are, respectively, the energy densities of the turbulent waves and of the ambient magnetic field, $\langle k\rangle$ is the average wave vector, and $\Omega_{\rm H}$ is the proton gyrofrequency.

Equation (8.2) can be solved numerically until an equilibrium state (that is, $\partial f/\partial t = 0$) is reached. The equilibrium electron spectra from the model are controlled by two parameters: the acceleration parameter $I_{\rm ACC}$ described above and the escape time τ. Above 10-20 keV, the collision and source terms in Eq. (8.2) can be neglected, and thus the equilibrium spectra depends in first approximation only on the product $I_\tau = I_{\rm ACC} \cdot \tau$.

Figure 8.4 show the equilibrium electron spectra for different values of $I_\tau = I_{\rm ACC} \cdot \tau$. As I_τ increases, the spectrum gets harder and harder. To explain the soft-hard-soft effect, we need either the acceleration or the trapping efficiency (or both) to increase until peak time, and then decrease again.

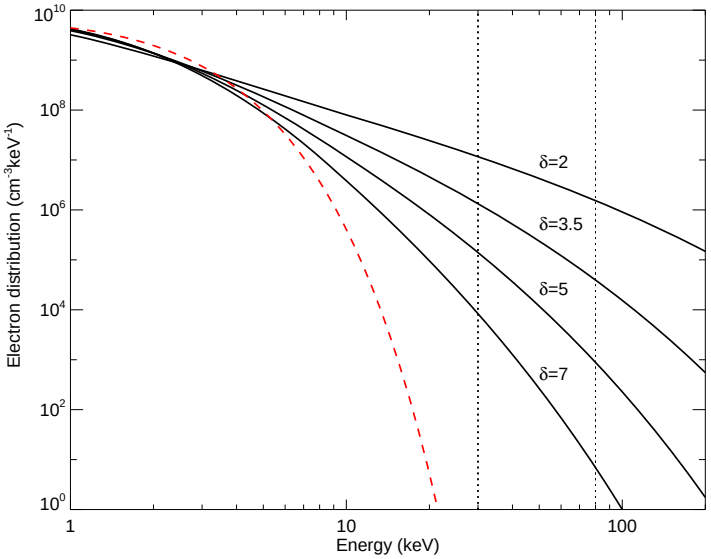

Fig. 8.4 Accelerated electron density distributions with different values of the power-law index resulting from changes in $I_\tau = I_{\rm ACC} \cdot \tau$. The dashed curve represents the ambient Maxwellian distribution. The two dotted lines indicate the energy range used for the computation of the power-law index δ shown above each spectrum. Harder spectra have a larger I_τ value (from Grigis and Benz 2006).

To see whether this produces the linear relation between the spectral index and the log of the flux normalization, Grigis and Benz (2006) computed the hard X-ray emission from these model electron spectra. Since these are equilibrium spectra, thin-target emission was computed. They then plotted the spectral index vs. the flux normalization of the resulting photon spectra. Since the spectra are not power-law, but bend down, they fit a power-law model to the model photon spectrum in a similar range as the one used for the observations.

Figure 8.5 shows the computed values for the spectral indices and flux normalizations for both the electron and the photon spectrum from the model. The results show that there is indeed a linear relation between the spectral index and the log of the flux normalization.

9 The connection between footpoint and coronal hard X-ray sources

Hard X-ray (HXR) sources at both footpoints of a coronal loop structure have been observed since Hoyng et al. (1981). As reviewed in Sections 1 & 2, they are understood to be thick-target bremsstrahlung emission produced by precipitating electrons, accelerated somewhere in or above the loop. A third HXR source situated above the looptop (looptop or coronal source) was first noted by Masuda et al. (1994) in *Yohkoh* observations. In simple solar flare models with reconnection and particle acceleration in the corona, we expect some relation between coronal HXR sources and footpoints. RHESSI has enabled us to study events featuring coronal sources and footpoint simultaneously. By studying the behavior of the sources in time and the relations between them, we can address questions like: Are both coronal and footpoint emissions caused by the same electron population? How is such an electron beam modified in the loop (collisions, return currents, etc.)? Is SHS behavior

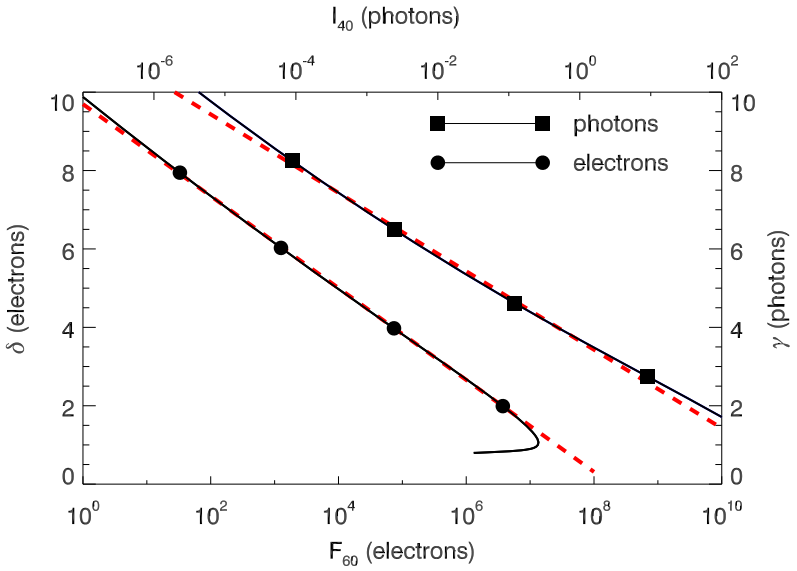

Fig. 8.5 Model results for the spectral index and flux normalization for electrons and photons. The dashed line is the best straight-line fit to the model results (in the range of spectral indices from 2 to 8 for the electrons, and 3 to 9 for the photons), corresponding to a pivot-point behavior (from Grigis and Benz 2006).

(Section 8.1) a transport effect produced by collisions or return currents, or is it a feature of the acceleration mechanism?

9.1 RHESSI imaging spectroscopy

RHESSI has provided the possibility of obtaining simultaneous, high-resolution imaged spectra at different locations on the Sun. One can therefore study each source separately in events with several contemporaneous HXR-sources. This high spectral resolution has allowed in many flares a reliable differentiation between thermal and nonthermal emission. RHESSI's imaging spectroscopy has allowed differences in individual flare source spectra and their evolution to be studied.

Sui et al. (2002) analyzed the C7.5 2002 February 20 limb flare showing two footpoint sources and a high above-the-looptop source in hard X-rays. Emslie et al. (2003) analyzed the X4.8 2002 July 23 flare with four HXR-sources observed by RHESSI. Emslie et al. found a coronal source with a strong thermal component, but the nonthermal component could not be studied due to severe pulse pile-up. Battaglia and Benz (2006) studied five M-class events. Due to the smaller pile-up amount in those events, studying the nonthermal coronal emission was possible. The results of these studies are summarized below.

9.2 Relation between the coronal source and footpoints

The quantitative relations between the footpoints and the coronal source and between the two footpoint can give information about the physical mechanisms at work in a solar flare.

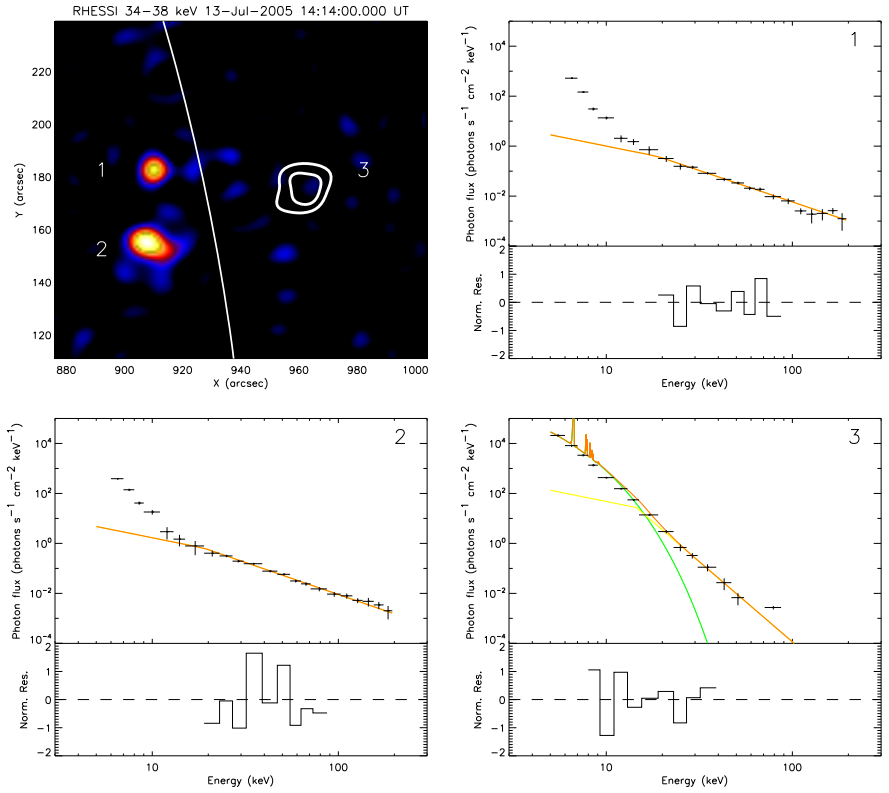

Fig. 9.1 *Top left* Image of a RHESSI event with three hard X-ray sources. The footpoints are visible on the solar disc. The position of the coronal source high above the limb is indicated by the 50 and 80% contours taken from a 10–12 keV image. *Illustrations 1-3* Respective spectra of the sources shown in the image (after Battaglia and Benz 2006).

Simple models envision a beam of accelerated electrons encountering a low-density region in the corona, which leads to thin-target bremsstrahlung. When the same electron beam reaches the chromosphere, the particles are fully stopped in the dense material, producing thick-target emission. Assuming an electron power-law distribution for the electron energy E of the form

$$F(E) = AE^{-\delta} \tag{9.1}$$

producing thin-target bremsstrahlung in the coronal source, the observed photon spectrum has spectral index $\gamma_{thin} = \delta + 1$ (equation 2.7). Reaching the chromosphere, the accelerated electrons will be fully stopped, producing thick-target bremsstrahlung with a photon spectral index $\gamma_{\rm thick} = \delta - 1$ (equation 2.8). In such a simple scenario one would therefore expect a difference in the photon spectral index $\gamma_{thin} - \gamma_{thick} = 2$ between the coronal source and the footpoints. Further, the two footpoints should be of equal hardness and intensity if one assumes a fully symmetric loop.

9.2.1 Observed difference between coronal and footpoint spectral indices

A sample of flares observed with *Yohkoh* to have coronal sources was studied by Petrosian et al. (2002). They found that the spectral index of the coronal sources was on the average steeper by 1 than the spectral indices of the footpoint sources. Sui et al. (2002) also found a spectral index difference of 1 for the 2002 February 20 flare observed with RHESSI.

Battaglia and Benz (2006) found that the coronal source was softer than both footpoints for all of their five events in nearly all analyzed time bins. Figure 9.1 (top left) shows a Clean image of an event on 2005 July 13 in the 34–38 keV energy band. The two footpoints are visible, as well as the 50 and 80% contours of the coronal source taken from a 10–12 keV image. Spectra and spectral fits are shown for the two footpoints and the coronal source. The steepness of spectrum of the coronal source (number 3 in the figure) relative to the spectra from the footpoints is apparent. However, the quantitative difference between the coronal source and footpoints often differed significantly from 2. The smallest mean difference, averaged over time, was 0.59 ± 0.24. The maximum mean difference, averaged over time, was 3.68 ± 0.14. These clearly contradict the theoretical expectation summarized above.

9.2.2 Differences between footpoints

Sui et al. (2002) found no significant difference in the spectral indices for the two footpoints in the 2002 February 20 flare. Piana et al. (2007) inverted count visibility spectra for this flare to obtain mean electron flux distributions for the footpoints. They found the mean electron flux distribution at the northern footpoint to be slightly steeper than that derived for the southern footpoint. The also found the distribution for the region between the footpoints (not the coronal source studied by Sui et al.) to be steeper than the footpoint distributions and to further steepen at energies above $\sim$60 keV.

Emslie et al. (2003) reported differences of 0.3-0.4 between the spectral indices of two footpoints in the event of 2002 July 23.

For the flares analyzed by Battaglia and Benz (2006), a significant difference was found in only one out of five events. For all other events, the mean difference in $\gamma_{\rm fp}$ was zero within the statistical uncertainty. Different spectra at the two footpoints imply an asymmetric loop. Such an asymmetry can result, for example, from different column densities or different beam fluxes and corresponding return current energy losses in the legs of the loop. It could also result from asymmetric magnetic trapping within the loop (e.g., Alexander and Metcalf 2002).

9.3 Spectral evolution in coronal sources

Previous observations of SHS spectral evolution (see Section 8.1) were made with full-Sun spectra which are typically dominated by footpoint emission. Battaglia and Benz (2006), in their imaging spectroscopy study, found that the coronal source itself shows SHS evolution. This is illustrated in Figure 9.2. This finding implies that SHS is not caused by transport effects within the flare loop, but is rather a property of the acceleration mechanism itself. Indeed, Grigis and Benz (2006) showed that SHS can be reproduced for electron spectra in a transit-time damping stochastic acceleration model (Section 8.2).

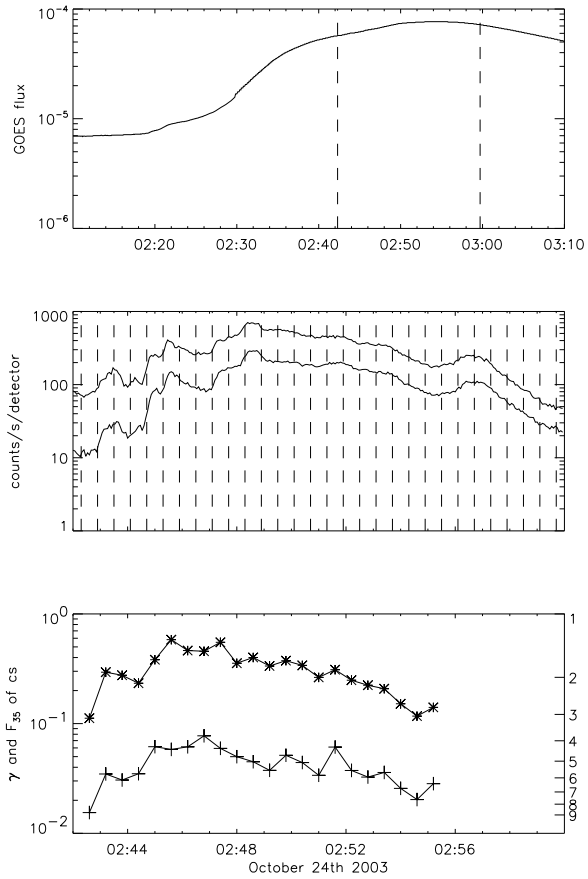

Fig. 9.2 *Top* GOES light curve of an event on 2003 October 24. *Middle* RHESSI 25–50 and 50–100 keV light curves. *bottom* Time evolution of fitted coronal source flux at 35 keV (F_{35}) and spectral index γ displaying SHS evolution (after Battaglia and Benz 2006).

9.4 Interpretation of the connection between footpoints and the coronal source

In the above account, emphasize was given to the difference in the spectral index between the coronal source and footpoints. Assuming a thin target in the corona and a thick target at the footpoints, one would expect a difference of two. However, the assumption of a pure thin target in the corona is often not justified. Veronig and Brown (2004) found coronal sources with very high column densities that act as thick targets for electrons of up to 60 keV.

As early as 1995, Wheatland and Melrose (1995) developed a simple 1-D (parallel propagating electrons) model, describing the coronal emission as intermediate thin-thick, depending on electron energy. In this model a high-density region ($\gtrsim 10^{12}$ cm^{-3}) is hypothesized to be present at or above the top of the flare loop. The model makes precise predictions for the shape of the coronal and footpoint spectra and the relations between them. Fletcher (1995) obtained Monte Carlo solutions to the Fokker-Planck equation to show that, with the inclusion of high electron pitch angles and collisional scattering, a compact coronal X-ray

source is produced at the top of a loop with a constant coronal density $\sim 3 \times 10^{10}$ cm^{-3}. Holman (1996) showed that, even in the simple 1-D model, a compact coronal source is produced when electrons are injected into a loop with a constant coronal density $\sim 2 \times 10^{11}$ cm^{-3} (see hesperia.gsfc.nasa.gov/sftheory/loop.htm). A compact coronal HXR source can also be produced if there is a compact magnetic trap at or above the top of the loop. Fletcher and Martens (1998) showed that, with such a trap, a significant coronal X-ray source can be produced at plasma densities as low as $\sim 4 \times 10^{9}$ cm^{-3}.

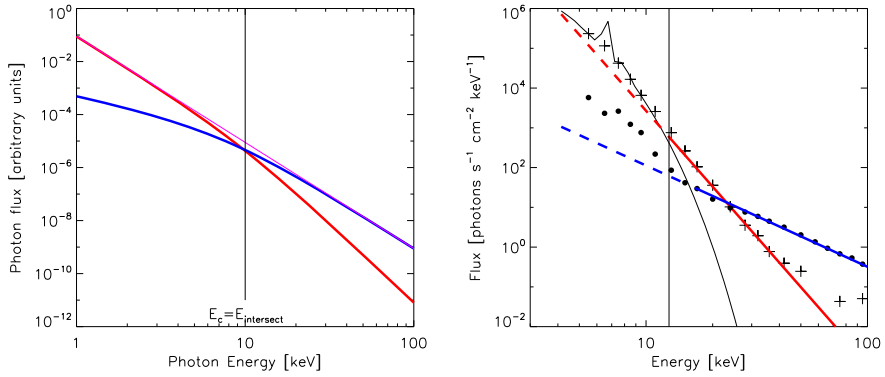

Fig. 9.3 *L*eft Model spectra for corona (red) and footpoints (blue) according to the model of Wheatland and Melrose (1995). *R*ight Observed RHESSI spectra for an event on 2003 October 24. Isothermal and power-law fits to the coronal (crosses) and footpoint (dots) spectra are shown. The vertical line indicates the critical energy for the transition between thin and thick target (after Battaglia and Benz 2007).

The left panel of figure 9.3 illustrates the model of Wheatland and Melrose (1995). The spatially integrated spectrum (violet) is the power-law spectrum (thick-target, $\gamma_{thick} = \delta - 1$) expected for a single-power-law electron distribution with no low- or high-energy cutoffs and no thermal component. For $\varepsilon \ll \sqrt{2KN}$ (see equation 2.3), the spectrum is dominated by thick-target radiation from the coronal source (red). There is a low-energy cutoff in the electron distribution at the footpoints at $E \sim \sqrt{2KN}$ because of the energy losses in the coronal source. The spectrum is dominated by thick-target radiation from the footpoints (blue) where $\varepsilon \gg \sqrt{2KN}$. It is in this regime that the radiation from the coronal source is thin-target and the spectral index of the coronal source is steeper by 2 than that of the footpoints. These spectra are characteristic of all the models reviewed above.

Sui et al. (2002) compared the RHESSI observations of the 2002 February 20 flare to a model with a constant-coronal-density loop and no magnetic trapping. They used a finite difference method (e.g., McTiernan and Petrosian 1990; Holman et al. 2002) to obtain steady-state solutions to the Fokker-Planck equation with collisional scattering and energy losses. Model images were convolved with the RHESSI response to produce simulated RHESSI observations for direct comparison with the February 20 flare images and imaged spectra. They found that, after obtaining a power-law model spectrum with an index of 3 that agreed with the observed footpoint spectra, the effective spectral index of the coronal source from the model (4.7) was significantly steeper than that obtained for the flare (4).

Battaglia and Benz (2007) compared the model of Wheatland and Melrose (1995) to the results of their study of five flares observed by RHESSI. The right panel of figure 9.3 shows observed spectra and spectral fits for one particular event. The observed spectra were

dominated by thermal coronal emission at low energies. Therefore, not all of the model predictions could be tested. However, the observed relations between the spectra did not agree with the predictions of the model. For the flare in figure 9.3, for example, the difference between the coronal source and footpoint spectral indices at the higher photon energies is 3.8 ± 0.1, not 2. Also, an estimate of the column density in the coronal source gives $\sqrt{2KN} \sim 10 - 15$ keV, while the intersection of the coronal and footpoint spectra is found to be at $\varepsilon \approx 23$ keV.

10 Identification of electron acceleration sites from radio observations

While energetic electrons excite hard X-ray emission during their precipitation into the dense layers of the solar atmosphere, they can also excite decimeter and meter wave radio emission during propagation and trapping in magnetic field structures in the dilute solar corona. The radio emission pattern in dynamic spectrograms can give information about the electron acceleration process, the locations of injection of electrons in the corona, and the properties of the coronal magnetoplasma structures.

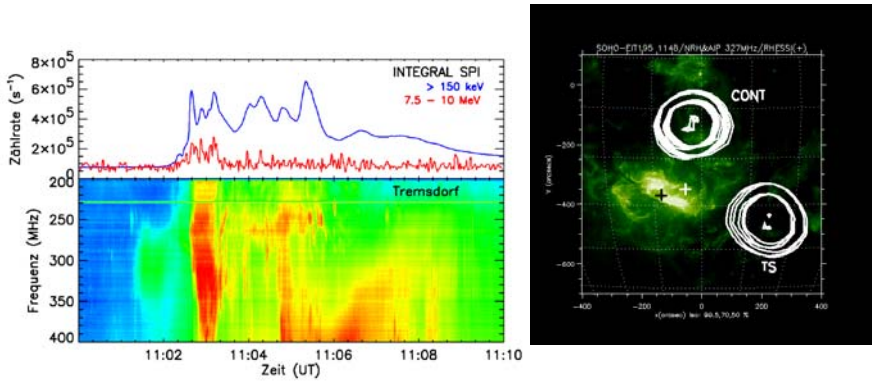

Fig. 10.1 The X17 2003 October 28 flare. *Left, bottom*: 200–400 MHz radio spectrum (Astrophysical Institute Potsdam) showing the signature of the outflow termination shock (TS, starting at 11:02:47 UT). *Left, top*: INTEGRAL count rates at 150 keV and 7.5–10 MeV. *Right*: radio source positions (Nançay Radio Heliograph, 327 MHz) overlaid on a SOHO-EIT image (11:47 UT 195 Å). The bright areas are EUV flare ribbons in AR10486. RHESSI HXR centroids are shown as "+". The integration times for the sources labeled TS and CONT are 11:02:45–11:03:15 UT and 11:13–11:17 UT, respectively (see Fig. 10.2).

Here we take as an example the X class flare on 2003 October 28. Different acceleration sites can be discriminated during the impulsive and the gradual flare phases. By combining radio spectral data from the Astrophysical Institute Potsdam (AIP, Mann et al. 1992), imaging data from the Nançay Radio Heliograph (NRH, Kerdraon and Delouis 1997) and hard X-ray (RHESSI, INTEGRAL) data, the occurrence time of a nondrifting, high-frequency type II radio burst signature in the radio spectrum is confirmed as a powerful electron acceleration stage. It yielded highly relativistic ($\gtrsim$10 MeV) electrons in the impulsive phase of the flare (Fig. 10.1, upper left). The radio spectrum suggests that this can be due to acceleration at the reconnection outflow termination shock (Aurass and Mann 2004), as predicted by the classical two-ribbon-flare model (Forbes 1986, Tsuneta and Naito 1998, Aurass et al.

2002). The radio source site is observed about 210 Mm to the SW of the flaring active region (TS in Fig. 10.1, right). In this direction, TRACE and SOHO-LASCO C2 images reveal dynamically evolving magnetoplasma structures in an erupting arcade (Aurass et al. 2006). For realistic parameters derived from these observations (the geometry, density, temperature, and low magnetic field values of ≈5 Gauss), Mann et al. (2006) demonstrated that a fully relativistic treatment of shock acceleration for the fast-mode outflow shock can explain the observed fluxes of energetic particles (see Vlahos et al 2008).

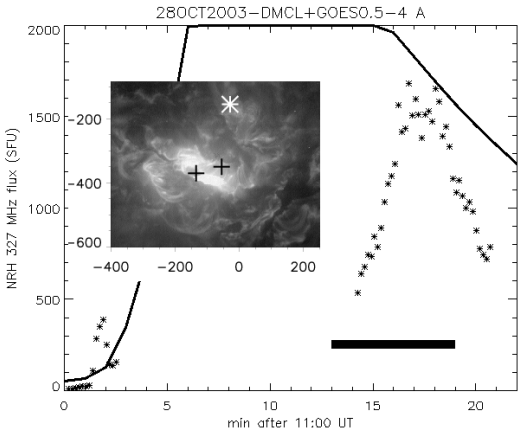

Fig. 10.2 Timing of the source CONT in Fig. 10.1: the NRH 327 MHz flux curve (in sfu, asterisks) versus the GOES flux curve (partly off-scale). Inset: SOHO-EIT image and radio source centroid as in Fig. 10.1. Thick bar: the start time of GeV-energy proton injection in space.

In the main flare phase of the same event, an additional radio source (CONT in Fig. 10.1) was found, indicating the presence of another acceleration site which acts for ≈ 15 min. Fig. 10.2 gives the timing and the source position with respect to the flaring active region. CONT is a m-dm-continuum source with fiber burst fine structure. Fiber bursts are excited by whistler waves propagating along field lines of the coronal magnetic field. As marked by a bold bar in the figure, the time of the CONT emission is also the start time of GeV proton injection in space. Aurass et al. (2006) have shown that this source site is not far from an open field (particle escape) region in the potential coronal magnetic field. The source briefly flashes up already in the early impulsive phase. Based on a new method of fiber burst analysis (Aurass et al. 2005; Rausche et al. 2007), Aurass et al. (2007) argue that this source most likely indicates acceleration at a contact between separatrix surfaces of different magnetic flux systems.

Radio observations of flares and their implications are further addressed in White et al (2008).

11 Discussion and Conclusions

11.1 Implications of X-ray observations for the collisional thick-target model

As discussed in Section 2, the core assumption of the collisional thick-target model is that the spatially integrated hard X-ray emission from nonthermal electrons is bremsstrahlung (free-free radiation) from electrons that lose all their suprathermal energy through collisional losses in the ambient plasma as they simultaneously radiate the hard X-rays. "Simultaneously" means within the observational integration time. This implies that all electrons that contribute significantly to the observed radiation reach a plasma dense enough or, more precisely, traverse a high enough column density for all of their suprathermal energy above the observed photon energies to be collisionally lost to the ambient plasma within the integration time. For typical $\gtrsim$1 s integration times, these conditions are met when the electrons stream downward from the corona into the increasingly dense plasma of the solar transition region and chromosphere.

Since the thick-target model is often implicit in our interpretation of the hard X-ray emission from flares, it is important to keep the underlying assumptions in mind and test the model while at the same time applying it to flare observations. We have discussed above several physical processes that, if significant, change the conclusions of the simple collisional thick-target model regarding the electron distribution produced in the acceleration region. These processes occur in either the thick-target region itself, or during the propagation of the electrons from the acceleration region to the thick-target. Only with the high spectral resolution and imaging of RHESSI has it become possible to observationally address these processes. Even with the RHESSI observations, however, it is difficult to conclusively determine the importance of each process.

A physical process that distorts the emitted X-ray spectrum is albedo (Section 3.4 and Kontar et al (2008)). Fortunately, the albedo contribution to the X-ray spectrum can be corrected on the assumption that the X-ray photons are isotropically emitted. This correction is available in the RHESSI spectral analysis software. If the photons are significantly beamed, however, the distortion of the spectrum can be substantially greater than that from isotropically emitted photons. An anisotropic photon distribution results from emitting electrons with an anisotropic pitch-angle distribution. The degree of anisotropy of the electron pitch-angle distribution also quantitatively affects conclusions from the thick-target model. Therefore, it is important to better determine the pitch-angle distribution of the emitting electrons and the contribution of albedo to the hard X-ray spectrum (see Kontar et al 2008).

The simple collisional thick-target model assumes that the target plasma is fully ionized. We have seen, however, that a nonuniformly ionized target region can produce an upward kink, or "chicane", in an otherwise power-law X-ray spectrum (Section 4). This spectral shift can provide a valuable diagnostic of the ionization state of the target plasma and its evolution. It is likely, however, that the power-law spectrum below the chicane is covered by thermal radiation. The chicane is then observed only as a downward break in the spectrum at energies above those dominated by the thermal emission. To distinguish this break from other causes of a spectral break, it is important to determine the contribution of nonuniform target ionization to flare X-ray spectra.

Return-current energy losses can also produce a downward break in the X-ray spectrum (Section 5). The break energy and shape of the spectrum depend on both the thermal structure of the plasma in the flare loop and on the nonthermal electron flux density distribution. These spectral modifications and their evolution throughout flares provide an important test for the presence of initially un-neutralized electron beams and the return currents they must

drive to neutralize them. Although RHESSI observations provide substantial information about the structure and evolution of flare spectra, only a weak lower limit on the electron flux density can usually be determined. Observations and analysis sufficiently comprehensive to verify the presence of return current energy losses are yet to be obtained.

A thorough comparison of flare spectra with theoretical spectra computed from models incorporating collisional and return current energy losses (including their effect on the angular distribution of the nonthermal electrons), as well as nonuniform target ionization and albedo, is still needed. Spectral fitting alone, however, is not likely to distinguish the importance of these different mechanisms. Comparison of the time evolution of the spectra with expectations would certainly enhance the success of such an endeavor.

The analysis of the evolution of X-ray source positions and sizes with photon energy and time provides another important test of the collisional thick-target model (Section 6). For these flares that show nonthermal source evolution in the corona and upper transition region, the source position and size are sensitive to the energy losses experienced by the nonthermal electrons. They are, in fact, sensitive to the very assumption that the sources are produced by electrons as they stream downward from an acceleration region higher in the corona. Further studies of the evolution of these coronal X-ray sources should substantially clarify the applicability of the collisional thick-target model.

For completeness we note that under some circumstances bound-free radiation may contribute significantly to the X-ray emission from nonthermal electrons. This possibility is discussed in Kontar et al (2008).

Another testable aspect of the collisional thick-target model is the heating of the flare plasma by the nonthermal electrons. If the flare plasma is primarily heated by these electrons and the thick-target region is primarily in the chromosphere and lower transition region, heating originating in the footpoints and expanding into the rest of the flare loop through "chromospheric evaporation" should be observed. On the other hand, if the loop is dense enough for the thick-target region to extend into the corona or if return-current heating is important, localized coronal heating should be observed.

It has generally been difficult to establish a clear connection between the location and evolution of hard X-ray sources produced by nonthermal electrons and thermal source regions. This is largely because of a lack of high-cadence images covering a broad range of coronal and transition region temperatures. Future studies of the coevolution of nonthermal X-ray sources and thermal sources in flares will be important in determining the extent to which heating mechanisms other than collisional heating by nonthermal electrons is significant.

Predicting the expected evolution of the heated plasma is hampered by insufficient knowledge of the dominant heat transport mechanisms. We have seen evidence that many flares cool by classical thermal conduction once the heating has subsided (Section 7.4), but this is not likely to be the dominant transport mechanism during rapid heating. Nevertheless, the spatial evolution of flare X-ray sources has so far been found to be consistent with chromospheric evaporation (Section 6.2). Also, the Neupert effect, observed in most flares, and Doppler shift measurements qualitatively support the thick-target model (Section 7.3), but these do not rule out the possibility of other heating mechanisms temporally correlated with the electron beam collisional heating. As discussed in Section 3, substantial progress has been made in deducing the energy flux (total power) carried by nonthermal electrons, but we usually can deduce only a lower limit on this energy flux. Continuing studies of flares similar to the 2002 April 15 flare and the initially cooler, early-impulsive flares (Section 3.5) may provide a better handle on this energy flux for comparison with thermal evolution. The

thermal properties, energetics, and evolution of flares is discussed further in Fletcher et al (2008).

11.2 Implications of X-ray observations for electron acceleration mechanisms and flare models

In Section 9 we addressed the X-ray spectra of hard X-ray sources sometimes observed above the top of the hot loops or arcades of loops observed in flares. We reviewed results indicating that the spectra are qualitatively, but not quantitatively consistent with expectations for electrons passing through a thin-target or quasi-thick-target region on their way to the thick-target footpoints of the flare loops. The apparent failure of these relatively simple models is probably a manifestation of the more complex above-the-looptop X-ray source structure revealed by RHESSI observations.

Before RHESSI, time-of-flight delays in hard X-ray timing indicated that electrons were accelerated in a region somewhat above the looptops of the hot flare loops in most flares (Section 7.1). Also, cusps were observed at the top of flare loops by *Yohkoh* (e.g., Section 9), indicating a magnetic connection to the region above the hot loops.

RHESSI images have revealed flares with double coronal sources, one at or just above the top of the hot loops and the other at a higher altitude above the lower source. The centroid of the lower source is higher in altitude at higher X-ray energies, while the centroid of the upper source is lower in altitude at higher X-ray energies, indicating that energy release occurred between these coronal sources (Sui and Holman 2003; Sui et al. 2004). In one flare the upper source accelerated outward to the speed of a subsequent coronal mass ejection. Both the Large Angle and Spectrometric Coronagraph (LASCO) on *SOHO* and the RHESSI observations have provided direct evidence for the presence of an extended, vertical current sheet above the hot flare loops and below the coronal mass ejection associated with eruptive flares (Ko et al. 2003; Lin et al. 2005; Sui et al. 2005b). These and related observations are discussed further in Fletcher et al (2008).

These recent observations strongly support the "standard" model of eruptive solar flares, in which the hot flare loops build up below a vertical current sheet where inflowing magnetic fields reconnect and a magnetic flux rope forms above the current sheet to become a coronal mass ejection (see Fletcher et al 2008; Vlahos et al 2008). Initially the current sheet may be small and associated with slow-mode shock waves, as in Petschek reconnection. Fast reconnection jets can stream upward and downward from the current sheet, likely ending in fast-mode shock waves where they run into slower magnetized plasma at the flare loop tops and the lower boundary of the magnetic flux rope (termination shocks). The pair of above-the-looptop X-ray sources may be associated with these fast-mode shock waves. We have described possible evidence for these shock waves from radio observations in Section 10.

The most difficult task is determining the dominant acceleration mechanism or mechanisms responsible for the energetic particles. The region above the flare loops contains or can contain quasi-DC electric fields, plasma turbulence, slow- and fast-mode shock waves, and collapsing magnetic traps, allowing for almost any acceleration mechanism imaginable. The problem is as much one of ruling out mechanisms as of finding mechanisms that work (cf. Miller et al. 1997). Acceleration mechanisms are addressed in Vlahos et al (2008).

In Section 8 we addressed the soft-hard-soft evolution of flare X-ray spectra. This spectral evolution could occur during the propagation of the electrons from the acceleration region to the thick-target footpoints. Return current losses, with their dependence on the electron beam flux (Section 5), for example, could be responsible for this evolution. However,

the observation that above-the-looptop sources show this spectral evolution (Section 9.3) indicates that it is a property of the acceleration process. We saw in Section 8.2 that the soft-hard-soft behavior can be reproduced in the acceleration region if the acceleration or trapping efficiency first increases and then decreases.

Flares displaying soft-hard-harder spectral evolution are of special interest, because they have been shown to be associated with high-energy proton events in space (Kiplinger 1995). What is the connection between the acceleration and release of energetic protons into space and X-ray spectral hardening late in flares? The answer to this question is important to both space weather prediction and understanding particle acceleration in flares.

References

D. Alexander and A. G. Daou, Astrophys. J. **666**, 1268 (2007).
D. Alexander and T. R. Metcalf, Solar Phys. **210**, 323 (2002).
S. K. Antiochos and P. A. Sturrock, Astrophys. J. **220**, 1137 (1978).
M. J. Aschwanden, *Physics of the Solar Corona. An Introduction*, Physics of the Solar Corona (2004).
M. J. Aschwanden, Astrophys. J. **661**, 1242 (2007).
M. J. Aschwanden and D. Alexander, Solar Phys. **204**, 91 (2001).
M. J. Aschwanden, J. C. Brown, and E. P. Kontar, Solar Phys. **210**, 383 (2002).
M. J. Aschwanden, R. M. Bynum, T. Kosugi, H. S. Hudson, and R. A. Schwartz, Astrophys. J. **487**, 936 (1997).
M. J. Aschwanden, T. Kosugi, H. S. Hudson, M. J. Wills, and R. A. Schwartz, Astrophys. J. **470**, 1198 (1996).
M. J. Aschwanden and R. A. Schwartz, Astrophys. J. **455**, 699 (1995).
M. J. Aschwanden, R. A. Schwartz, and D. M. Alt, Astrophys. J. **447**, 923 (1995).
M. J. Aschwanden, R. A. Stern, and M. Güdel, ArXiv e-prints **710** (2007).
H. Aurass and G. Mann, Astrophys. J. **615**, 526 (2004).
H. Aurass, G. Mann, G. Rausche, and A. Warmuth, Astron. Astrophys. **457**, 681 (2006).
H. Aurass, G. Rausche, and G. Mann, Astron. Astrophys. in press (2007).
H. Aurass, G. Rausche, G. Mann, and A. Hofmann, Astron. Astrophys. **435**, 1137 (2005).
H. Aurass, B. Vršnak, and G. Mann, Astron. Astrophys. **384**, 273 (2002).
M. Battaglia and A. O. Benz, Astron. Astrophys. **456**, 751 (2006).
M. Battaglia and A. O. Benz, Astron. Astrophys. **466**, 713 (2007).
M. Battaglia, P. C. Grigis, and A. O. Benz, Astron. Astrophys. **439**, 737 (2005).
S. G. Benka and G. D. Holman, Astrophys. J. **435**, 469 (1994).
A. O. Benz, Astrophys. J. **211**, 270 (1977).
J. W. Brosius and G. D. Holman, Astrophys. J. Lett. **659**, L73 (2007).
J. C. Brown, Solar Phys. **18**, 489 (1971).
J. C. Brown, Solar Phys. **28**, 151 (1973).
J. C. Brown, M. J. Aschwanden, and E. P. Kontar, Solar Phys. **210**, 373 (2002).
J. C. Brown, A. G. Emslie, G. D. Holman, C. M. Johns-Krull, E. P. Kontar, R. P. Lin, A. M. Massone, and M. Piana, Astrophys. J. **643**, 523 (2006).
J. C. Brown, A. G. Emslie, and E. P. Kontar, Astrophys. J. Lett. **595**, L115 (2003).
J. C. Brown and J. M. Loran, Mon. Not. Roy. Astron. Soc. **212**, 245 (1985).
P. J. Cargill, J. T. Mariska, and S. K. Antiochos, Astrophys. J. **439**, 1034 (1995).
E. W. Cliver, B. R. Dennis, A. L. Kiplinger, S. R. Kane, D. F. Neidig, N. R. Sheeley, Jr., and M. J. Koomen, Astrophys. J. **305**, 920 (1986).
J. L. Culhane, A. T. Phillips, M. Inda-Koide, T. Kosugi, A. Fludra, H. Kurokawa, K. Makishima, C. D. Pike, T. Sakao, and T. Sakurai, Solar Phys. **153**, 307 (1994).
B. R. Dennis, Solar Phys. **100**, 465 (1985).
B. R. Dennis and D. M. Zarro, Solar Phys. **146**, 177 (1993).
S. V. D'Iakonov and B. V. Somov, Solar Phys. **116**, 119 (1988).
A. G. Emslie, Astrophys. J. **235**, 1055 (1980).
A. G. Emslie, Astrophys. J. Lett. **595**, L119 (2003).
A. G. Emslie, E. P. Kontar, S. Krucker, and R. P. Lin, Astrophys. J. Lett. **595**, L107 (2003).
A. G. Emslie, H. Kucharek, B. R. Dennis, N. Gopalswamy, G. D. Holman, G. H. Share, A. Vourlidas, T. G. Forbes, P. T. Gallagher, G. M. Mason, T. R. Metcalf, R. A. Mewaldt, R. J. Murphy, R. A. Schwartz, and T. H. Zurbuchen, Journal of Geophysical Research (Space Physics) **109**, 10104 (2004).
M. W. Ewell, Jr., H. Zirin, J. B. Jensen, and T. S. Bastian, Astrophys. J. **403**, 426 (1993).
G. H. Fisher and S. L. Hawley, Astrophys. J. **357**, 243 (1990).
L. Fletcher, Astron. Astrophys. **303**, L9+ (1995).
L. Fletcher and H. S. Hudson, Solar Phys. **210**, 307 (2002).
L. Fletcher and P. C. H. Martens, Astrophys. J. **505**, 418 (1998).
L. Fletcher et al, Space Sci. Rev. XXX (2008).
T. G. Forbes, Astrophys. J. **305**, 553 (1986).
K. J. Frost and B. R. Dennis, Astrophys. J. **165**, 655 (1971).
W. Q. Gan, Astrophys. Spa. Sci. **260**, 515 (1998).
W. Q. Gan, Y. P. Li, and J. Chang, Astrophys. J. **552**, 858 (2001).
P. C. Grigis and A. O. Benz, Astron. Astrophys. **426**, 1093 (2004).
P. C. Grigis and A. O. Benz, Astron. Astrophys. **434**, 1173 (2005).

P. C. Grigis and A. O. Benz, Astron. Astrophys. **458**, 641 (2006).
S. Hayakawa and K. Kitao, Progress of Theoretical Physics **16**, 139 (1956).
G. D. Holman. In: *Bulletin of the American Astronomical Society*, Vol. 28 of *Bulletin of the American Astronomical Society*939 (1996).
G. D. Holman, Astrophys. J. **586**, 606 (2003).
G. D. Holman, L. Sui, J. McTiernan, and V. Petrosian. In: P. C. H. Martens and D. Cauffman (eds.): *Multi-Wavelength Observations of Coronal Structure and Dynamics*405 (2002).
G. D. Holman, L. Sui, R. A. Schwartz, and A. G. Emslie, Astrophys. J. Lett. **595**, L97 (2003).
P. Hoyng, A. Duijveman, M. E. Machado, D. M. Rust, Z. Svestka, A. Boelee, C. de Jager, K. T. Frost, H. Lafleur, G. M. Simnett, H. F. van Beek, and B. E. Woodgate, Astrophys. J. Lett. **246**, L155+ (1981).
H. S. Hudson. In: *Bulletin of the American Astronomical Society*, Vol. 23 of *Bulletin of the American Astronomical Society*1064 (1991).
H. S. Hudson and F. Fárník. In: J. Kuijpers (ed.): *ESA Special Publication*, Vol. 506 of *ESA Special Publication*261 (2002).
S. R. Kane and K. A. Anderson, Astrophys. J. **162**, 1003 (1970).
J. Kašparová, M. Karlický, E. P. Kontar, R. A. Schwartz, and B. R. Dennis, Solar Phys. **232**, 63 (2005).
J. Kašparová, E. P. Kontar, and J. C. Brown, Astron. Astrophys. **466**, 705 (2007).
A. Kerdraon and J.-M. Delouis. In: G. Trottet (ed.): *Coronal Physics from Radio and Space Observations*, Vol. 483 of *Lecture Notes in Physics, Berlin Springer Verlag*192 (1997).
A. L. Kiplinger, Astrophys. J. **453**, 973 (1995).
J. W. Knight and P. A. Sturrock, Astrophys. J. **218**, 306 (1977).
Y.-K. Ko, J. C. Raymond, J. Lin, G. Lawrence, J. Li, and A. Fludra, Astrophys. J. **594**, 1068 (2003).
E. P. Kontar and J. C. Brown, Advances in Space Research **38**, 945 (2006).
E. P. Kontar, J. C. Brown, A. G. Emslie, R. A. Schwartz, D. M. Smith, and R. C. Alexander, Astrophys. J. Lett. **595**, L123 (2003).
E. P. Kontar, J. C. Brown, and G. K. McArthur, Solar Phys. **210**, 419 (2002).
E. Kontar et al, Space Sci. Rev. XXX (2008).
N. A. Krall and A. W. Trivelpiece, *Principles of plasma physics*, International Student Edition - International Series in Pure and Applied Physics, Tokyo: McGraw-Hill Kogakusha, 1973 (1973).
J. Leach and V. Petrosian, Astrophys. J. **269**, 715 (1983).
J. Lin, Y.-K. Ko, L. Sui, J. C. Raymond, G. A. Stenborg, Y. Jiang, S. Zhao, and S. Mancuso, Astrophys. J. **622**, 1251 (2005).
R. P. Lin, B. R. Dennis, G. J. Hurford, D. M. Smith, A. Zehnder, P. R. Harvey, D. W. Curtis, D. Pankow, P. Turin, M. Bester, A. Csillaghy, M. Lewis, N. Madden, H. F. van Beek, M. Appleby, T. Raudorf, J. McTiernan, R. Ramaty, E. Schmahl, R. Schwartz, S. Krucker, R. Abiad, T. Quinn, P. Berg, M. Hashii, R. Sterling, R. Jackson, R. Pratt, R. D. Campbell, D. Malone, D. Landis, C. P. Barrington-Leigh, S. Slassi-Sennou, C. Cork, D. Clark, D. Amato, L. Orwig, R. Boyle, I. S. Banks, K. Shirey, A. K. Tolbert, D. Zarro, F. Snow, K. Thomsen, R. Henneck, A. McHedlishvili, P. Ming, M. Fivian, J. Jordan, R. Wanner, J. Crubb, J. Preble, M. Matranga, A. Benz, H. Hudson, R. C. Canfield, G. D. Holman, C. Crannell, T. Kosugi, A. G. Emslie, N. Vilmer, J. C. Brown, C. Johns-Krull, M. Aschwanden, T. Metcalf, and A. Conway, Solar Phys. **210**, 3 (2002).
R. P. Lin and R. A. Schwartz, Astrophys. J. **312**, 462 (1987).
R. P. Lin, R. A. Schwartz, R. M. Pelling, and K. C. Hurley, Astrophys. J. Lett. **251**, L109 (1981).
W. Liu, S. Liu, Y. W. Jiang, and V. Petrosian, Astrophys. J. **649**, 1124 (2006).
G. Mann, H. Aurass, W. Voigt, and J. Paschke. In: C. Mattok (ed.): *Coronal Streamers, Coronal Loops, and Coronal and Solar Wind Composition*, Vol. 348 of *ESA Special Publication*129 (1992).
G. Mann, H. Aurass, and A. Warmuth, Astron. Astrophys. **454**, 969 (2006).
A. M. Massone, A. G. Emslie, E. P. Kontar, M. Piana, M. Prato, and J. C. Brown, Astrophys. J. **613**, 1233 (2004).
S. Masuda, T. Kosugi, H. Hara, S. Tsuneta, and Y. Ogawara, Nature **371**, 495 (1994).
J. M. McTiernan and V. Petrosian, Astrophys. J. **359**, 524 (1990).
J. A. Miller, P. J. Cargill, A. G. Emslie, G. D. Holman, B. R. Dennis, T. N. LaRosa, R. M. Winglee, S. G. Benka, and S. Tsuneta, J. Geophys. Res. **102**, 14631 (1997).
J. A. Miller, T. N. Larosa, and R. L. Moore, Astrophys. J. **461**, 445 (1996).
R. O. Milligan, P. T. Gallagher, M. Mathioudakis, D. S. Bloomfield, F. P. Keenan, and R. A. Schwartz, Astrophys. J. Lett. **638**, L117 (2006)a.
R. O. Milligan, P. T. Gallagher, M. Mathioudakis, and F. P. Keenan, Astrophys. J. Lett. **642**, L169 (2006)b.
N. Nitta, B. R. Dennis, and A. L. Kiplinger, Astrophys. J. **353**, 313 (1990).
G. K. Parks and J. R. Winckler, Astrophys. J. Lett. **155**, L117+ (1969).
V. Petrosian, T. Q. Donaghy, and J. M. McTiernan, Astrophys. J. **569**, 459 (2002).

M. Piana, A. M. Massone, G. J. Hurford, M. Prato, A. G. Emslie, E. P. Kontar, and R. A. Schwartz, Astrophys. J. **665**, 846 (2007).
M. Piana, A. M. Massone, E. P. Kontar, A. G. Emslie, J. C. Brown, and R. A. Schwartz, Astrophys. J. Lett. **595**, L127 (2003).
G. Rausche, H. Aurass, G. Mann, M. Karlický, and C. Vocks, Solar Phys. in press (2007).
P. Saint-Hilaire and A. O. Benz, Astron. Astrophys. **435**, 743 (2005).
D. M. Smith, R. P. Lin, P. Turin, D. W. Curtis, J. H. Primbsch, R. D. Campbell, R. Abiad, P. Schroeder, C. P. Cork, E. L. Hull, D. A. Landis, N. W. Madden, D. Malone, R. H. Pehl, T. Raudorf, P. Sangsingkeow, R. Boyle, I. S. Banks, K. Shirey, and R. Schwartz, Solar Phys. **210**, 33 (2002).
L. Sui and G. D. Holman, Astrophys. J. Lett. **596**, L251 (2003).
L. Sui, G. D. Holman, and B. R. Dennis, Astrophys. J. **612**, 546 (2004).
L. Sui, G. D. Holman, and B. R. Dennis, Astrophys. J. **626**, 1102 (2005)a.
L. Sui, G. D. Holman, and B. R. Dennis, Astrophys. J. Lett. **645**, L157 (2006).
L. Sui, G. D. Holman, and B. R. Dennis, Astrophys. J. **670**, in press (2007).
L. Sui, G. D. Holman, B. R. Dennis, S. Krucker, R. A. Schwartz, and K. Tolbert, Solar Phys. **210**, 245 (2002).
L. Sui, G. D. Holman, S. M. White, and J. Zhang, Astrophys. J. **633**, 1175 (2005)b.
E. Tandberg-Hanssen and A. G. Emslie, *The physics of solar flares*, Cambridge and New York, Cambridge University Press, 1988, 286 p. (1988).
S. Tsuneta and T. Naito, Astrophys. J. Lett. **495**, L67+ (1998).
M. Väänänen and S. Pohjolainen, Solar Phys. **241**, 279 (2007).
A. Veronig, M. Temmer, A. Hanslmeier, W. Otruba, and M. Messerotti, Astron. Astrophys. **382**, 1070 (2002)a.
A. Veronig, B. Vršnak, B. R. Dennis, M. Temmer, A. Hanslmeier, and J. Magdalenić, Astron. Astrophys. **392**, 699 (2002)b.
A. Veronig, B. Vršnak, M. Temmer, and A. Hanslmeier, Solar Phys. **208**, 297 (2002)c.
A. M. Veronig and J. C. Brown, Astrophys. J. Lett. **603**, L117 (2004).
A. M. Veronig, J. C. Brown, B. R. Dennis, R. A. Schwartz, L. Sui, and A. K. Tolbert, Astrophys. J. **621**, 482 (2005).
N. Vilmer, G. Trotter, and S. R. Kane, Astron. Astrophys. **108**, 306 (1982).
N. Vilmer et al, Space Sci. Rev. XXX (2008).
L. Vlahos et al, Space Sci. Rev. XXX (2008).
M. S. Wheatland and D. B. Melrose, Solar Phys. **158**, 283 (1995).
S. White et al, Space Sci. Rev. XXX (2008).
R. M. Winglee, A. L. Kiplinger, D. M. Zarro, G. A. Dulk, and J. R. Lemen, Astrophys. J. **375**, 366 (1991).
Y. Xu, A. G. Emslie, and G. J. Hurford, Astrophys. J. **673**, in press (2008).
V. V. Zharkova and M. Gordovskyy, Astron. Astrophys. **432**, 1033 (2005).
V. V. Zharkova and M. Gordovskyy, Astrophys. J. **651**, 553 (2006).

Index